

AD-A050 054

LOCKHEED MISSILES AND SPACE CO INC PALO ALTO CALIF PA--ETC F/6 20/5
EXPERIMENTAL STUDY OF THE INITIATION MECHANISM OF LASER SUPPORT--ETC(U)
NOV 77 T E SHARP

UNCLASSIFIED

LMSC-D566093

AFOSR-TR-78-0068

NL

1 OF 1
AD-A050054



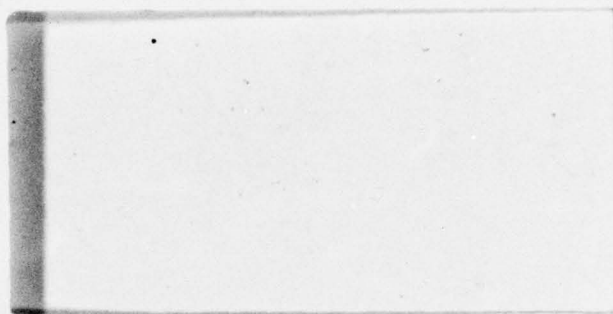
END
DATE
FILMED
3-78
DDC

AFOSR-TR- 78 - 0068

2

AD A050054

AD No. _____
DDC FILE COPY



DDC
RECEIVED
FEB 15 1978
B

LOCKHEED

MISSILES & SPACE COMPANY, INC. • SUNNYVALE, CALIFORNIA
A SUBSIDIARY OF LOCKHEED AIRCRAFT CORPORATION

Approved for public release;
distribution unlimited.

**AIR FORCE OFFICE OF SCIENTIFIC RESEARCH (AFSC)
NOTICE OF TRANSMITTAL TO DDC**

This technical report has been reviewed and is
approved for public release IAW AFR 190-12 (7b).
Distribution is unlimited.

A. D. BLOSE
Technical Information Officer

2

9 Final Report, 1 Jan 75-30 Sep 77,

EXPERIMENTAL STUDY OF THE INITIATION
MECHANISM OF LASER SUPPORTED
ABSORPTION WAVES.

by

10 T. E. Sharp

14 LMSC-D566093

11 November 1977

12 77P

15

For the Period

1 January 1975 - 30 September 1977

for

Air Force Office of Scientific Research

Contract Number F44620-75-C-0041

15

18 AFOSR 19 TR-78-0068

Nuclear Sciences Laboratory
Lockheed Palo Alto Research Laboratory
3251 Hanover Street
Palo Alto, California 94304

16 2301
17 A5

DDC
RECEIVED
FEB 15 1978
B

Q7

DISTRIBUTION STATEMENT A
Approved for public release;
Distribution Unlimited

210 118 JOB

REPORT DOCUMENTATION PAGE		READ INSTRUCTIONS BEFORE COMPLETING FORM
1. REPORT NUMBER AFOSR-TR- 78 - 0068	2. GOVT ACCESSION NO.	3. RECIPIENT'S CATALOG NUMBER
4. TITLE (and Subtitle) EXPERIMENTAL STUDY OF THE INITIATION MECHANISM OF LASER SUPPORTED ABSORPTION WAVES	5. TYPE OF REPORT & PERIOD COVERED FINAL 1 January 1975 thru 30 September 1977	
	6. PERFORMING ORG. REPORT NUMBER	
7. AUTHOR(s) T. E. Sharp	8. CONTRACT OR GRANT NUMBER(s) F44620-75-C-0041✓	
9. PERFORMING ORGANIZATION NAME AND ADDRESS Lockheed Missiles & Space Company, Inc. Palo Alto Research Laboratory 3251 Hanover Street, Palo Alto, CA 94304	10. PROGRAM ELEMENT, PROJECT, TASK AREA & WORK UNIT NUMBERS 2301/AS 61102F	
11. CONTROLLING OFFICE NAME AND ADDRESS Air Force Office of Scientific Research INP Bldg. 410, Bolling AFB, Washington, DC 20332	12. REPORT DATE 28 November 1977	
	13. NUMBER OF PAGES 75	
14. MONITORING AGENCY NAME & ADDRESS (If different from Controlling Office)	15. SECURITY CLASS. (of this report) Unclassified	
	15a. DECLASSIFICATION/DOWNGRADING SCHEDULE	
16. DISTRIBUTION STATEMENT (of this Report) <div style="border: 1px solid black; padding: 5px; width: fit-content; margin: 10px auto;">DISTRIBUTION STATEMENT A Approved for public release; Distribution Unlimited</div>		
17. DISTRIBUTION STATEMENT (of the abstract entered in Block 20, if different from Report)		
18. SUPPLEMENTARY NOTES		
19. KEY WORDS (Continue on reverse side if necessary and identify by block number) Laser - Supported Absorption Waves Laser - Supported Detonation Waves Laser Interaction with Materials Plasma Diagnostics		
20. ABSTRACT (Continue on reverse side if necessary and identify by block number) Mechanisms for prompt initiation of laser supported absorption waves are identified with their experimental consequences. A phenomenological theory of electron emission from metals under intense laser irradiation is discussed. A recent model for initiation of laser supported detonation waves which requires exceeding both irradiation and fluence thresholds is summarized. Design, construction, and testing of an apparatus including a target to		

(Continued)

permit measurement of electron emission with fast time resolution and an electron energy spectrograph and detector system are described.

Experiments with 0.3 μ s pulses of 10.6 μ m laser light with peak irradiance from 0.5 to 10 Mw/cm² on stainless steel, titanium alloy, and aluminum targets in vacuum are reported. Data are given for the peak current density of electron emission as a function of laser irradiance. Roughening of the aluminum surface was found to increase electron emission and large emission currents were produced on an aluminum-coated multipoint microarray.

Experiments with 0.1 ns pulses of 1.06 μ m laser light with peak irradiance from 8 to 250 Mw/cm² on various aluminum targets in vacuum are described. Data are given for the time dependence and peak current density of electron emission as a function of laser irradiance and for the dependence of electron emission on laser polarization.

In the experiments reported here, sufficient electron current density to produce LSD waves in air is generated in vacuum at laser irradiances near the reported thresholds. The temperature rise is too small for thermionic emission to be significant except possibly at the highest irradiances studied. The temperature rise is too small to induce vaporization of even thin laminae of the bulk material. The slope of log total electron emission versus log irradiance plots is too small to correspond to true multiphoton emission of electrons. The bulk of the evidence supports enhanced field emission at surface protrusions as an operative mechanism for electron production in most of the materials studied.

ACCESSION for		
NTIS	White Section	<input checked="" type="checkbox"/>
DDC	Buff Section	<input type="checkbox"/>
UNANNOUNCED		<input type="checkbox"/>
JUSTIFICATION		
BY		
DISTRIBUTION/AVAILABILITY CODES		
Dist.	AVAIL.	and/or SPECIN.
A		

UNCLASSIFIED

SUMMARY

This final report describes the work completed through the third year of the contract for an experimental investigation into the basic mechanism for formation of prompt laser supported absorption waves (LSAW) created when laser pulses of high power density are directed onto target surfaces in air. The objective of the research is to provide a detailed understanding of the laser-surface interaction, under conditions when bulk vaporization does not occur, by examination of the properties of the ejected electrons emitted in vacuum. Both 1.06 μm and 10.6 μm lasers were used in this study.

As technical background, four mechanisms for prompt initiation of LSAW were considered - localized vaporization of absorptive inclusions in the surface, thermionic emission, localized high-field electron emission from protrusions on the surface, and multiphoton emission of electrons. Experimental tests to distinguish among these mechanisms were identified. A preliminary correlation of previous studies of electron emission under intense laser radiation due to Musal was used to identify true multiphoton emission of electrons, a transition region, and a saturation region as a function of increasing laser irradiance. A two-criterion model for production of laser supported detonation (LSD) waves due to Musal was explored. The model requires exceeding a minimum irradiation threshold, to eject enough energetic electrons from the target to seed an ionization cascade in the air, and also exceeding a minimum fluence threshold for development of a nearly fully ionized plasma.

The design, construction, and testing of the target chamber and vacuum system, the target developed for measurements with fast time response of total electron emission, and the electron energy analyzer and detector are presented in detail. Q-switched laser pulses were obtained from both the CO_2

laser and the Nd laser and focused to yield irradiances in excess of the minimum irradiance criterion for production of LSD waves. Target materials included chemically polished pure aluminum, aluminum 6061-T6 and 2024-T3 alloys, cast aluminum, type 321 stainless steel, titanium Ti-6Al-4V alloy, gold, silver, and painted aluminum.

Experiments were conducted in vacuum with 0.3 μ s pulses of 10.6 μ m laser light with incident irradiances from 0.3 to 10 Mw/cm² on metal targets. The peak electron current density from type 321 stainless steel and Ti-6Al-4V titanium alloy increased with irradiance but showed no break at the threshold irradiance for initiation of LSD waves. Electron emission from aluminum was found to increase substantially upon roughening of the target surface. An even larger emission was found upon irradiation of an array of aluminum coated field emission points. For polished pure aluminum, 6061-T6 aluminum alloy, gold, silver, and painted aluminum targets, electron emission was not observed, but upper limits for electron current density at irradiances of 5 Mw/cm² were found to be less than 8×10^{-5} A/cm².

Experiments were conducted with 0.1 ns pulses of 1.06 μ m laser light with irradiances from 8 to 250 Mw/cm² on various aluminum targets in vacuum. The time dependence of electron emission changed from a sharp spike at low irradiances to a pulse with a slower rise and longer decay at the highest irradiance. Rotation of the polarization vector of the laser light to be perpendicular to the target surface increased the electron emission from aluminum alloy but had no effect on cast aluminum. Measurements of peak current density versus irradiance showed electron emission from cast aluminum to be the same as that from chemically polished pure aluminum. Roughening the surface of aluminum alloy increased the electron emission at this wavelength also. Emission from aluminum 2024-T3 alloy was found to be much smaller than that from aluminum 6061-T6 alloy.

In the experiments reported here, sufficient electron current density to produce LSD waves in air is generated in vacuum at laser irradiances near

the reported thresholds. The temperature rise is too small for thermionic emission to be significant except possibly at the highest irradiances studied. The temperature rise is too small to induce vaporization of even thin laminae of the bulk material. The slope of log total electron emission versus log irradiance plots is too small to correspond to true multiphoton emission of electrons. The bulk of the evidence supports enhanced field emission as an operative mechanism for electron production in most of the materials studied.

ACKNOWLEDGMENTS

The author expresses his gratitude to Dr. Henry M. Musal, Jr., for suggesting the research, for sharing his theoretical insight, and for permission to quote from his work. The invaluable assistance of Dr. Bruce Watson with the conduct of the experiments is gratefully acknowledged. Thanks are also due to Homer Norris, Richard Nightingale, and Barton Mass for help with the experiments. Special thanks are due to Dr. Jack Longfellow of Western Electric Laboratories for loan of the Q-switch for the CO₂ laser.

TABLE OF CONTENTS

<u>Section</u>		<u>Page</u>
	SUMMARY	ii
	ACKNOWLEDGMENTS	v
	LIST OF FIGURES	viii
	LIST OF TABLES	ix
1	INTRODUCTION	1-1
2	TECHNICAL BACKGROUND	2-1
	2.1 Mechanisms for Prompt Initiation of LSAW	2-1
	2.2 Electron Emission from Metals under Intense Laser Irradiation	2-7
	2.3 Model for Initiation of Laser-Supported Detonation Waves	2-12
3	APPARATUS AND EXPERIMENTAL PROCEDURE	3-1
	3.1 Target Chamber and Vacuum System	3-1
	3.2 Target for Measurement of Total Electron Emission	3-2
	3.3 Electron-Energy Spectrograph and Detector	3-4
	3.3.1 Design Considerations	3-4
	3.3.2 Detector Considerations	3-6
	3.3.3 Hardware	3-8
	3.3.4 Calibration	3-10
	3.3.5 Modification	3-14
	3.4 CO ₂ 10.6 μ m Laser	3-16
	3.4.1 Experimental Apparatus	3-16
	3.4.2 CO ₂ 10.6 μ m Laser, Experimental Parameters	3-21

<u>Section</u>		<u>Page</u>
	3.5 1.06 μm Laser Pulse Characteristics	3-23
	3.5 Target Materials	3-24
4	RESULTS AND DISCUSSION	4-1
	4.1 Experiments at 10.6 μm	4-1
	4.1.1 Stainless Steel	4-2
	4.1.2 Titanium Alloy	4-2
	4.1.3 Aluminum-Containing Materials	4-5
	4.1.4 Other Materials	4-6
	4.2 Experiments at 1.06 μm	4-6
	4.2.1 Time Dependence of Electron Emission	4-8
	4.2.2 Polarization Dependence of Electron Emission	4-8
	4.2.3 Total Emission Studies on Various Materials	4-12
	4.3 Discussion	4-16
	4.3.1 Estimate of Electron Current Density Required to Initiate Fast Breakdown in Air	4-16
	4.3.2 Temperature Rise at the Target Surface	4-17
	4.3.3 Effects of Temperature Rise	4-21
	4.3.4 Multiphoton Emission of Electrons	4-22
	4.3.5 Enhanced Field Emission	4-23
	4.3.6 Conclusions	4-23
5	REFERENCES	5-1

LIST OF FIGURES

<u>Figure</u>		<u>Page</u>
2-1	Electron Emission from Metals under Intense Laser Radiation	2-10
3-1	Fast Response Target Assembly	3-3
3-2	Schematic Diagram of Experimental Arrangement	3-9
3-3	Scale Diagram of Electron Energy Spectrograph and Detector Assembly	3-11
3-4	Tuning of the Electron Energy Spectrograph	3-12
3-5	Dispersion of the Electron Energy Spectrograph	3-13
3-6	Calibration of Electron Energy Spectrograph	3-15
3-7	Energy Spectrogram of Electron Distribution from Laser Pulse on Al Alloy Showing Spurious Bright Spot	3-15
3-8	Schematic Diagram of Experimental Arrangement for Experiments with Q-switched pulses from the CO ₂ Laser	3-18
4-1	Dependence of Electron Emission from Type 321 Stainless Steel on Laser Irradiance at 10.6 μm	4-3
4-2	Dependence of Electron Emission from Titanium Alloy on Laser Irradiance of 10.6 μm	4-4
4-3	Scanning Electron Micrograph of Multipoint Array Irradiated at 10.6 μm a. 200X b. 500X	4-7
4-4	Oscilloscope Traces of Total Electron Emission versus Time at Different Irradiances (1.06 μm , 0.1 ns pulses)	4-9
4-5	Polarization Effect on Electron Emission - Al 6061-T6	4-10
4-6	Polarization Effect on Electron Emission - Cast Aluminum	4-11

<u>Figure</u>		<u>Page</u>
4-7	Dependence of Electron Emission on Laser Irradiance - Pure Aluminum (Etched) and Cast Aluminum	4-13
4-8	Dependence of Electron Emission on Laser Irradiance - Al 6061-T6 "as received" and abraded	4-14
4-9	Dependence of Electron Emission on Laser Irradiance - "as received" aluminum alloys - 6061-T6 and 2024-T3	4-15

LIST OF TABLES

<u>Table</u>		<u>Page</u>
2-1	Experimental Tests and Predicted Results for Various Mechanisms for Initiation of LSAW	2-8
4-1	Properties of Target Materials and Estimates of Temperature Rise	4-19

Section 1
INTRODUCTION

This final report describes the work completed through the third year of the contract for an experimental investigation into the basic mechanism for formation of prompt laser supported absorption waves created when laser pulses of high power density are directed onto target surfaces. The objective of the research is to provide a detailed understanding of the laser-surface interaction, under conditions when bulk vaporization does not occur, by examination of the properties of the ejected electrons.

In Section 2 a discussion of the technical background and current state of knowledge is given. Section 3 is devoted to the development of *apparatus and experimental procedure*. Section 4 contains experimental results and discussion.

Section 2

TECHNICAL BACKGROUND

This section contains a description of the phenomenon of prompt initiation of laser-supported absorption waves (LSAW), the initiation mechanisms which have been proposed, and some possible experimental tests to distinguish among these mechanisms. Next there is a discussion of a preliminary correlation of previous studies of electron emission from metal surfaces under intense laser radiation. Finally, a new model for initiation of laser-supported detonation waves is described.

2.1 Mechanisms for Prompt Initiation of LSAW

The phenomenon of prompt initiation of laser-supported detonation waves from metal surfaces has now been observed by many experimenters. Typical are the experiments at Battelle, (C. T. Walters, et al., Reference 1), where fractional microsecond laser bursts of $10.6 \mu\text{m}$ photons from a CO_2 TEA laser on rolled Al surfaces in ambient air have produced laser supported absorption waves (LSAW) which travel through the air away from the target. The luminous waves absorb laser radiation, blocking delivery of energy to the target. The power density of the laser for these experiments is in the range $50\text{--}500 \text{ Mw/cm}^2$, with a pulse length of 200 ns. Onset of the air breakdown is observed within 20 ns after the laser pulse reaches peak power. The LSAW are initiated in a time much too short to produce bulk vaporization of the surface. Streak photographs of the surface-air interface during the laser pulse show the breakdown emanating as streamers from a few randomly distributed discrete points on the surface (at threshold power density, 10-50 points in the 1 cm^2 laser spot). Increasing the laser power density increases the number of source points and the density of the streamers. At the highest laser power densities, the breakdown appears to spread uniformly over the entire illuminated spot on the surface. Flashing the same spot re-

repeatedly may produce an absorption wave on the first pulse but no absorption waves on subsequent pulses. Examination of the surface of aluminum sheet stock of the type used in the experimental studies, using a scanning electron microscope, showed localized randomly distributed pits, scratches, protrusions, and inclusions that could be the sites for "prompt" absorption wave initiation. Although electron microscopic examination of the surface after laser irradiation reveals removal of some surface features, opening of pits, and so forth, looking at the "before" photographs gave essentially no clues as to which features would serve as sources of LSAW or which features would be changed by the laser flash. Once the laser absorption wave has been initiated, its propagation can be explained by relatively well understood mechanisms of laser absorption producing cascade ionization of the air. Therefore, interest is focused on the mechanism which initiates the breakdown.

Many mechanisms were initially proposed including vaporization of the surface, oxide films, chemical reactions and several others, but on careful examination, (P. D. Thomas, H. M. Musal, References 2,3), most were disqualified as sources of rapid initiation of LSAW. There are currently four viable mechanisms which could conceivably account for rapid production of ionization at localized sites, from which an absorption wave could be quickly initiated:

- (1) Localized vaporization of inclusions which may have higher absorptivity than the surrounding metal surface and poor thermal contact with the bulk of the metal leading to a plasma "micro-jet" of the inclusion material.
- (2) Thermionic emission from "hot-spots" associated with surface imperfections.
- (3) Localized high-field electron emission from protrusions on the surface.
- (4) Multiphoton emission of electrons from the metal surface.

The probability of initiation of LSAW by localized vaporization of inclusions is highly dependent on the nature of the impurity inclusions. There is no doubt that this mechanism is theoretically possible if the appropriate thermally isolated impurities are present in the target surface. Studies of this mechanism should give special attention to the chemical composition and distribution of surface impurities.

Preliminary theoretical evaluation of thermionic emission showed that thermal conduction in the target would lead to low emission yields and that, in addition, space charge limitations would severely restrict the amount of ionization that could be achieved. Initiation by thermionic emission is, therefore, improbable unless the imperfection is a thermally isolated thin lamina. For this case, Musal has shown that if the lamina has a thickness of only a few electromagnetic skin depths, then thermionic emission of electrons from the lamina could produce initiation of LSAW within the short times observed experimentally, (Thomas, Musal, and Y. S. Chou, Reference 3b).

P. D. Thomas and H. M. Musal (Reference 2b) have examined theoretically the high-field emission mechanism in detail. Field emission of electrons from metal surfaces requires electric fields of 20-30 MV/cm. The fields attained in the Battelle laser experiments are only about 0.2 MV/cm. Field emission of electrons is therefore not expected to occur from the flat surface of the metal. However, Musal has calculated that surface protrusions, modeled as prolate spheroids with height-to-base diameter aspect ratio of 20, experience an electric field intensification of a factor of 100, which is sufficient to produce field emission of electrons. Treating the laser field as quasistatic, he has calculated that such field-emitted electrons could experience potentials of about 10 eV in the vicinity of protrusions which are less than 1 μ m high. Electrons produced by field emission can be accelerated by the laser field to high enough energy to cause impact ionization of the ambient air molecules, thus creating an air plasma and negating the effect of space charge limitation. The time scale for ionization buildup via this phenomenon appears to be consistent with the experimentally observed effects

of "prompt" absorption wave initiation at high incident beam intensities, (e.g., within 50 ns for laser power densities of 100 Mw/cm^2).

Additional calculations (Thomas, Musal and Chou, Reference 3) on the field emission mechanism have produced some interesting results. The original calculations assumed a step function form for the laser pulse. The calculated time required to produce initiation of an absorption wave was much shorter than the time observed experimentally at high laser power density. Modification of the calculation to include a reasonable non-zero risetime brings the calculated initiation time into good agreement with the observations. In addition, there is known to be a synergistic effect between temperature and field emission. A temperature rise of a few hundred degrees can produce an orders-of-magnitude increase in field emission currents. Consideration of both these effects leads to theoretically calculated initiation times in very good agreement with the experimental observations.

To infer the correct mechanism, one must identify features which differ in the theoretical models and select those which are most susceptible to experimental verification.

The energies of the electrons ejected from the surface differ for these mechanisms. Thermionic electrons have energies of a few tenths of an eV. Electrons produced from vaporization of impurities should have energies characteristic of plasma temperatures, that is a few eV at most. Electrons produced by field ionization may have energies of 10 eV or more. High energy electrons have been observed in multiphoton photoelectric effect studies (Gy. Farkas, I. Kertesz, Zs. Naray and P. Varga, Reference 4). Measurement of the energy distribution of the ejected electrons is a powerful method for distinguishing among the proposed mechanisms.

Another significant difference among the initiation mechanisms is the time history of electron ejection. Both thermionic emission and vaporization of surface impurities occur through an absorption and heat transfer process.

A definite delay should be observable in the onset of electron production, and electrons should continue to be emitted after termination of the laser pulse - both due to thermal lag. Field emission currents, on the other hand, are a highly nonlinear function of laser power density. The electron current should therefore rise steeply as the peak of the laser pulse is reached and should fall more steeply than the fall-off of the laser pulse. This effect has also been observed experimentally in the transition from the multiphoton photoelectric effect to thermionic emission. (Gy. Farkas, et al., Reference 4). If the laser pulse is made very short, field emission could still occur in phase with the pulse, but electron production from the other mechanisms would be unimportant (Gy. Farkas, et al., Reference 5).

The magnitude of the electric field perpendicular to the target surface strongly influences the probability of electron emission. Consequently, the polarization of the laser beam has a large effect on the current from optical field emission (Gy. Farkas, Zs. Naray and P. Varga, Reference 6). For a beam striking a metal surface at a glancing angle, maximum electron emission was observed when the electric field was polarized in the plane of incidence. This direction yields the largest net electric field perpendicular to the surface and thus produces the largest force for ejection of electrons. Negligible electron current was produced with polarization parallel to the surface. If the power absorption of the target is normalized to correct for changes in reflectivity with polarization, changes in the angle of polarization should have no effect on electron production by vaporization of impurities. At fixed polarization, the magnitude of the electric field will vary as the sine of the angle of incidence at the target. The area illuminated will increase as the secant of the angle of incidence, so that the heating per unit area will behave as the cosine of the angle of incidence. At constant laser power density, field emission currents from the target will show a sine function dependence, increasing with the angle of incidence, but currents from vaporization of impurities should show a cosine dependence, decreasing as the angle of incidence is increased (both at fixed polarization).

More detailed discussion of the theoretical treatment of LSAW may be

found in the report by Thomas and Musal (Reference 2b) from which the following conclusions and recommendations are taken:

Several mechanisms for rapid production of ionization at a material surface from which a laser-supported absorption wave could be promptly initiated prior to uniform surface vaporization have been discussed. It has been shown that high-field electron emission from surface irregularities appears to be a viable contender; however, localized vaporization at material inhomogeneities has not been ruled out.

A critical difference between these mechanisms resides in whether the initial ionization consists of a material vapor plasma "micro-jet" or an ambient atmospheric gas "plasmoid". Both types of plasmas will radiate; hence measurement of the radiation spectra potentially could be used to differentiate between them. Fast time resolution (on the order of tens of nanoseconds) and high spatial resolution (on the order of tens of microns) are required if a material vapor micro-jet initiates the LSAW because there will also be atmospheric radiation from the absorption wave within a very short time and within a small distance from the surface. On the other hand, if it is electron emission that initiates the LSAW, there could be subsequent vaporization of the surface material after the LSAW has been launched, which would produce a material vapor spectrum. Therefore, time and/or space integrated spectra do not appear to be adequate to resolve this distinction.

It has already been pointed out that the distinguishing characteristic of the field-emission mechanism for prompt initiation of laser-supported absorption waves is the acceleration of the emitted electrons in the high field region near the emitting surface to energies sufficiently high as to cause impact ionization of the ambient atmosphere. Therefore, a critical test of this mechanism would be to measure the energies of the electrons emanating from a surface under intense laser irradiation. This experiment should be done in a vacuum rather than in an ambient atmosphere so that the electrons do not lose energy through inelastic collisions with the atmospheric molecules before they reach the energy measuring detector. This will not

alter the basic mechanism because an ambient atmosphere does not play a fundamental role in the emission and acceleration process. Thermal electron production processes, such as vaporization or thermionic emission, are also expected to produce electrons under these conditions. However, the mean energy of such electrons will be a few electron-volts at most, whereas the field-emission and subsequent acceleration mechanism is expected to produce electrons with energies above ten electron-volts. Thus, a measurement of the electron energy distribution should distinguish between the two types of sources and verify the presence of a high energy group that could cause impact ionization if an ambient atmosphere were present.

The phenomena being studied operate on a microscale in both time and space. Furthermore, these phenomena are very non-linearly dependent on the incident radiation intensity. Any temporal "spike" or spatial "hot spot" in the incident beam intensity will greatly enhance the initiation mechanism because of the strong nonlinear dependence of field-emission current density and cascade-ionization buildup on the electric field intensity.

In summary, experimental tests which can be used to distinguish among the suggested initiation mechanisms are listed in Table 2-1 together with the predicted result for each mechanism.

2.2 Electron Emission from Metals under Intense Laser Irradiation

Electron emission from metal surfaces under intense laser irradiation has been observed, measured, and reported by many investigators, notably Farkas et al., (Reference 8), Knecht, (Reference 9), Logothetis and Hartman, (Reference 10), Ahmad and Walsh, (Reference 11), and Bechtel, Smith, and Bloembergen, (Reference 12, 13). Initial assessment of the measurements of these investigators reveals apparently conflicting results and unexplained trends in the data. It now appears, however, that it may be possible to reconcile all these results into an overall phenomenological picture. This approach, which was formulated by H. M. Musal, will be briefly outlined here.

Table 2-1
Experimental Tests and Predicted Results
for
Various Mechanisms for Initiation of Laser Supported Absorption Waves

EXPERIMENTAL VARIABLE	MECHANISM			PREDICTED RESULT	
	THERMIONIC EMISSION	VAPORIZATION OF IMPURITIES	FIELD EMISSION	MULTI-PHOTON EMISSION	
ELECTRON ENERGY (MEASURED)	LOW	MEDIUM	HIGH	MEDIUM	
TIME OF ELECTRON EMISSION (MEASURED)	DELAYED	DELAYED	PROMPT	PROMPT	
SHORT LASER PULSE (HIGH IRRADIANCE, LOW FLUENCE)	NO EMISSION	NO EMISSION	EMISSION	EMISSION	
POLARIZATION OF LASER BEAM, CORREC- TED FOR ABSORPTION	NO EFFECT	NO EFFECT	MAXIMUM AT └ TO SURFACE	MAXIMUM AT └ TO SURFACE	
SURFACE CLEANLINESS	MINOR	CRUCIAL	MINOR	MINOR	
SURFACE ROUGHNESS	MINOR	MINOR	CRUCIAL	MINOR	
WAVELENGTH, CORRECTED FOR TOTAL ABSORPTION	MINOR	MINOR	CRUCIAL	CRUCIAL	

Figure 2-1 shows, in a semi-quantitative manner, how the electron emission current from a laser-irradiated metal surface behaves as the intensity of the radiation is increased. The emission current density J is plotted versus the laser irradiance G (both on normalized logarithmic scales). The dominant feature of this schematic graph is the transition threshold at which the emission current increases markedly. This transition threshold irradiance has been arbitrarily located at unity on the normalized intensity scale.

At irradiances below the transition, the electron emission current obeys a true "multi-photon" photoelectric emission law; the emission current density increases with irradiance according to the relationship $J \sim G^n$, where n = integer value of $[1 + (\phi/h\nu)]$, ϕ is the work function of the metal surface, and $h\nu$ is the photon energy of the laser radiation. In this region the plot is a straight line with slope n . Several lines are drawn to show the effect of increasing work function within the constraint of constant n . In this regime the emission current is sensitive to the polarization of the laser radiation, and the emitted electrons appear to have medium to high energies (up to the order of 10 electron-volts).

At the transition intensity the electron emission increases with a slope of order ~ 15 , which is to be compared to a typical slope of 2 or 3 (for ruby lasers) at the lower intensities. The current is observed to increase by many orders of magnitude. In this transition region the data display some sensitivity to the work function, but no data have been reported on the effects of polarization of the laser beam or on the energies of the emitted electrons.

At much higher irradiances the current density appears to display a saturation effect with the slope of the curve approaching unity.

With the above qualitative picture in mind, the experimental observations cited earlier can be put into context. This is shown in the figure

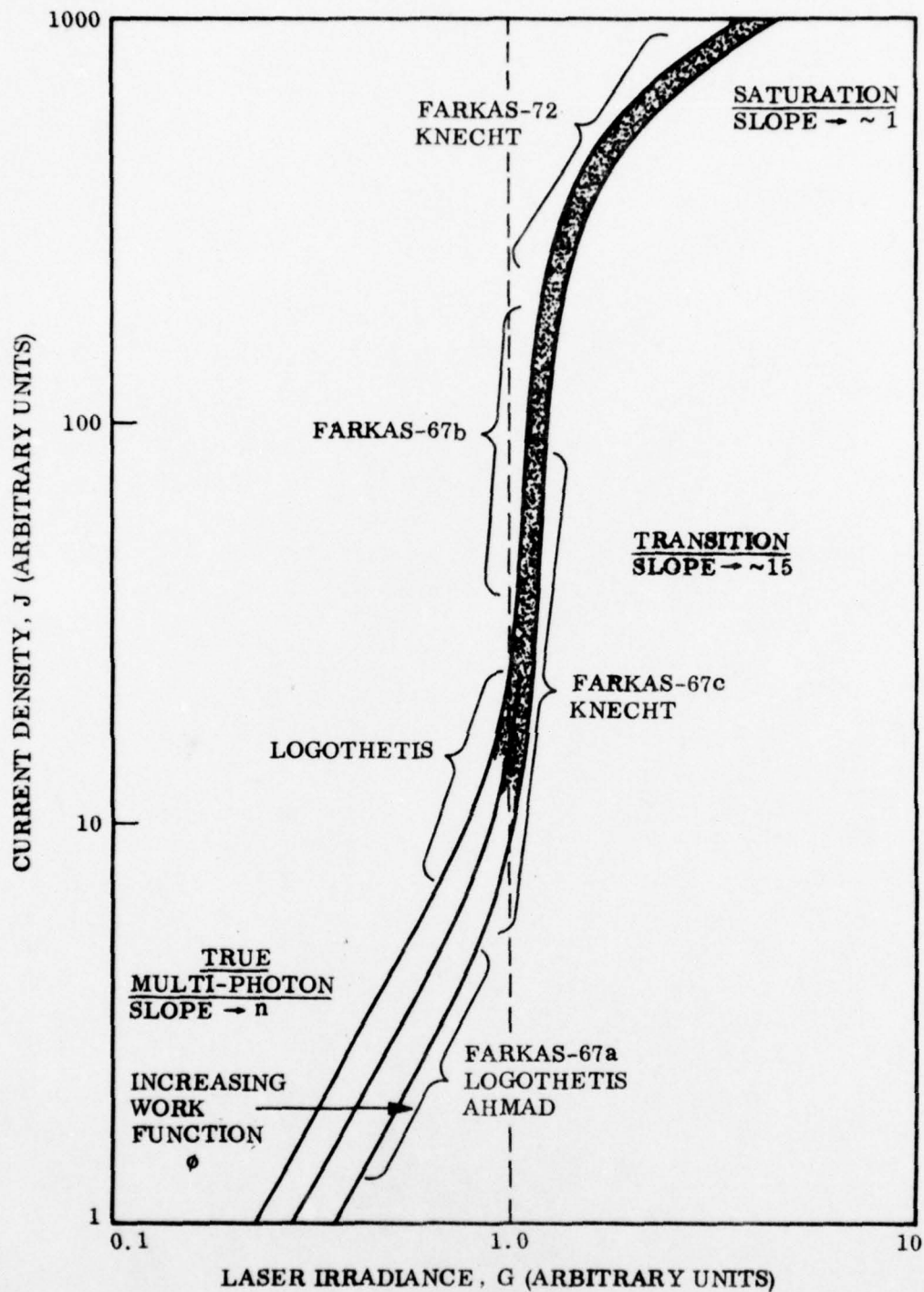


Fig. 2-1. Electron Emission from Metals under Intense Laser Radiation. The results of various investigators are correlated and located in the appropriate emission regimes: "true" multi-photon, transition, and saturation. For details, see text.

by assignment of each observation to its appropriate regime. Thus, the data of Farkas - 67a, (Reference 6), on sensitivity of the electron emission to polarization of the laser radiation and the data of Logothetis and Hartman, (Reference 10), and of Ahmad and Walsh, (Reference 11), on the slope of the emission current curve, all fall in the true multi-photon emission regime and are consistent with each other. Some of the data obtained by Farkas - 67c, (Reference 7), by Knecht, and by Logothetis and Hartman span the intensity range between the true multi-photon emission regime and the transition regime. The data of Farkas - 67b, (Reference 4), falls totally within the highly non-linear transition regime. Finally, the saturation regime is appropriate to the data obtained by Farkas - 72 (Reference 8), and by Knecht (Reference 9). Most of the results cited above were obtained by using ruby laser although a very limited set of results were obtained with Nd:glass lasers and frequency-doubled ruby laser radiation. For ruby laser radiation, the incident threshold irradiance for the abrupt transition appears to be approximately $1 \text{ to } 3 \times 10^6 \text{ watt/cm}^2$.

Recent work by Bechtel, Smith and Bloembergen (Reference 12), has employed single picosecond pulses of frequency doubled (532 nm) light from a Nd:YAG laser. For tantalum, molybdenum, and tungsten they found the maximum electron current density to be proportional to the square of the maximum irradiance as expected for a two-photon process. In the case of tantalum this second-order behavior extended to the highest irradiances investigated - about $5 \times 10^8 \text{ watt cm}^{-2}$ producing a current density of about $1.5 \text{ ampere cm}^{-2}$. The transition and saturation regions were not yet reached at the maximum irradiance of these experiments.

Four-photon photoemission from tungsten was studied by Bechtel, Smith and Bloembergen, (Reference 13), using 30 picosecond, $1.06 \mu\text{m}$ pulses from a Nd:YAG laser. The electron current density was found to be proportional to the fourth power of the irradiance over the range $0.4 \text{ to } 4 \times 10^9 \text{ watt cm}^{-2}$. The electron current density at the highest irradiance was about $1.5 \times 10^3 \text{ A cm}^{-2}$. The authors concluded that the use of short pulses made possible the

verification of the four-photon process. For longer pulses, the contributions from thermally induced processes usually become significant. The thermally induced contributions would increase the slope of the log emission versus log irradiance curve to higher values at the large irradiances, and it would be difficult to identify unambiguously a single high-order multiphoton process.

A theoretical framework based on a generalized Fowler-DuBridge theory of electron photoemission appears promising (Reference 12). The basic assumption is that the total electron current density is a sum of partial current densities, each of which has a simple form, either one- or n-photon photoemission or thermionic emission. Numerical solutions of the heat conduction equation for the surface temperature as a function of space and time have been calculated (Bechtel, Reference 14), and a theoretical expression covering one- and n-photon photoemission is also available (Reference 13). Unfortunately, even for pure metals with ideal surfaces, "the uncertainties in the electron escape probability, the escape depth, and the n-photon absorption coefficient are large and no accurate calculation. . . is presently possible" (Reference 13).

Nevertheless, the consolidation of available experimental data on electron emission from laser-irradiated metal surfaces into an overall phenomenological picture is useful although it requires further work for verification. In particular, the location of the transition threshold at various laser wavelengths and as a function of laser pulse length is crucial to the development of wavelength scaling relationships, and more metals of engineering importance need to be studied.

2.3 Model for Initiation of Laser-Supported Detonation Waves

A model for the initiation of laser-supported detonation waves (LSDW) and its correlation with experimental data has been developed by Musal (Reference 15). By plotting the characteristics of all laser pulses which were reported to produce LSDW, he discovered two requirements for the

production of these waves:

- 1) a minimum irradiation (power density) threshold, and
- 2) a minimum fluence (energy density) threshold. Both thresholds must be exceeded to produce LSDW. Neither the delivery of a very short, high power pulse nor the delivery of a large amount of energy in a long, low power pulse is sufficient to initiate a detonation wave.

The irradiation criterion requires that the power density of the laser pulse must exceed both of two values, one related to the properties of the target and the other based on the properties of air. The irradiation threshold for metallic targets is 2.5×10^5 watt/cm² absorbed by the material. This is presumably the minimum irradiance required to eject enough energetic electrons from the target to seed an ionization cascade in the air close to the target. The irradiation threshold for subsequent growth of a fast, non-equilibrium ionization cascade in air is $(1 \times 10^6 \text{ watt/cm}^2)(10.6 \text{ } \mu\text{m}/\lambda)^2$, where λ is the wavelength of the laser.

The fluence criterion requires that the energy density of the laser pulse be sufficient for full development of the air plasma from a low electron density to the high electron density of a nearly fully ionized plasma. The fluence threshold is $(1 \text{ J/cm}^2)(10.6 \text{ } \mu\text{m}/\lambda)^2(1 \text{ atm}/P)$ where P is the ambient pressure.

Musal's two-criterion model gives a good fit to the existing LSDW data. A plot of fluence versus irradiance in the laser pulse provides a useful framework for correlating the existing experiments, and it has considerable predictive value. This is a significant achievement. It should be noted, however, that in its present form the model is fitted to observed gross data and does not deal in quantitative detail with the underlying physical processes. In particular, the mechanism of electron emission from the target is unspecified as is the mechanism by which the electrons acquire sufficient

energy to initiate ionization. Additional experimental and theoretical work should refine the model.

An especially interesting aspect of the model is the wavelength scaling of the irradiation threshold. With CO_2 laser radiation $10.6 \mu\text{m}$, the material-dependent value ($2.5 \times 10^5 \text{ watt/cm}^2$ absorbed) and the intrinsic absorptivity of aluminum ($\alpha = 0.03$) lead to a threshold of $1.2 \times 10^7 \text{ watt/cm}^2$ incident irradiance, to be compared with the air-dependent threshold of $1 \times 10^6 \text{ watt/cm}^2$ incident irradiance. With the Nd:glass laser at $1.06 \mu\text{m}$, the material-dependent threshold based on the absorptivity of aluminum at this wavelength ($\alpha = 0.06$) becomes $4 \times 10^6 \text{ watt/cm}^2$, to be compared with the air-dependent threshold of $1 \times 10^8 \text{ watt/cm}^2$. Thus, for aluminum subjected to pulses from the CO_2 laser, the irradiance threshold governing LSDW initiation should be material-dependent; but for pulses from the Nd:glass laser, the governing threshold should be dependent on the power density requirement for creating a fast cascade in the air.

Section 3

APPARATUS AND EXPERIMENTAL PROCEDURE

The initiation mechanism for laser supported absorption waves was studied by irradiating the target in vacuum and making measurements on the emitted electrons. The measurements were planned to include determination, as a function of laser power density and wavelength, of the yield of electrons, the energy spectrum, the dependence on polarization, the dependence on angle of incidence, and the dependence on time during the pulse. Measurements were made on various metals of practical importance and on surfaces deliberately prepared to contain a larger number of field emission points, to contain a large concentration of absorptive inclusions, or to be relatively pure and flat.

In 3.1 the target chamber and vacuum system are described followed in 3.2 by a description of the target developed for measurements with fast time response of total electron emission. The design, construction, calibration, and modification of the electron energy analyzer and detector are presented in 3.3. A description of the 10.6 μm CO_2 laser and experimental procedure is presented in 3.4. The 1.06 μm Nd laser pulse characteristics are given in 3.5. Finally, the target materials are described in 3.6.

3.1 Target Chamber and Vacuum System

The target chamber and vacuum system were designed and built in the first-year phase of the contract. Their characteristics are described below.

The target chamber is an aluminum cylinder 9 inches high by 12 inches outer diameter. It contains four 2 inch ports for attachment of optical element, viewing window, and electrical feed throughs. ZnSe optics were chosen for the CO_2 laser studies because of their broad band transmission (visible to CO_2 wavelengths). A single-element glass lens is used for the

Nd:Glass laser studies. The lid of the target chamber is a box-like "top hat" which contains the electron spectrograph, the channel electron multiplier array with phosphor output, and fiber optics to bring the resultant signal outside the vacuum system to be photographed. The target chamber contains the target positioner which permits externally controlled displacement of the target by $\pm 1/4$ inch in each of x-, y-, and z-directions and rotation through 360° . Two different types of target holders are in use, one which can be biased reliably for the electron energy measurements, and one which forms part of a transmission line for fast time measurements of electron pulses.

The vacuum system employs Viton O-rings and can reach a base pressure of 3×10^{-7} torr. A 4-inch gate valve isolates the target chamber from the pumping train which consists of a liquid-nitrogen chilled baffle (Varian NRC0316-4), a 4-inch diffusion pump with cold cap (Varian NRCM4), and a direct-drive mechanical pump (Leybold-Heraeus D8A). The pressure is monitored by a thermocouple gauge for the higher pressure ranges and an ionization gauge for pressures below 10^{-4} torr (both run by a Granville Phillips type 270 Gauge Controller).

The target chamber and vacuum system are supported on a nearly cubical (24 x 24 x 29 inches) aluminum support table fitted with casters for easy movement to different laser facilities. Once the table is roughly positioned to place the laser beam close to the target, final adjustments can be made with positioners integral to the table. These permit motion of the target chamber for leveling and vertical adjustment (± 1 inch), side-to-side motion (± 1 inch), and rotation ($\pm 5^\circ$). These features were designed to simplify the initial setup of the target chamber at any laser facility.

3.2 Target for Measurement of Total Electron Emission

The fast response target shown in Fig. 3-1 was designed to match a 50 ohm line and appears electrically to be an open circuit when viewed from

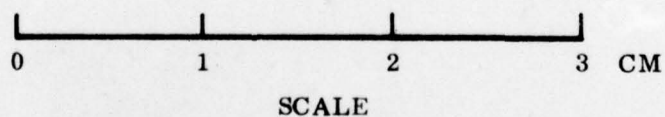
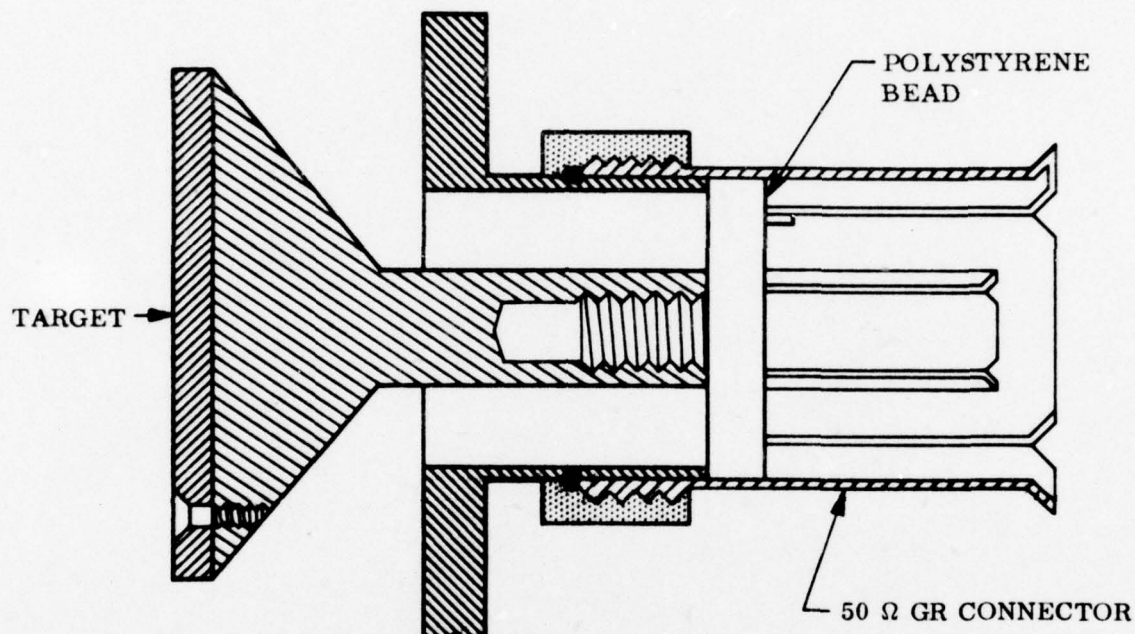


Fig. 3-1. Fast Response Target Assembly. Designed as an open-ended section of 50 ohm transmission line to minimize stray reactances.

the connector end. The design formula for a 50 ohm line is given by (Ref. 16)

$$\tan\left(\frac{1}{2}\theta_2\right) = \exp(5\sqrt{k}/6) \tan\left(\frac{1}{2}\theta_1\right) \quad (3.1)$$

where k is the dielectric constant of the line to be matched ($k = 2.0$ for teflon), θ_1 is the half-angle for the inner conical conductor and θ_2 is the half-angle for the outer conical conductor. For ease of construction θ_2 was chosen to be 90° ; thus θ_1 becomes 47° . The target assembly was constructed to fit into half of a General Radio Type 874 50 ohm connector. In use an adapter connects the GR connector to 3 mm solid copper shielded 50 ohm line, to a 3 mm type connector through the wall of the vacuum chamber, and on to the Tektronix 7904 oscilloscope.

To register a voltage signal at the scope from the electrons ejected by a laser pulse on the target, it was necessary to create a small drawout (of the order of 10 V/cm) field at the target face. A planar electrode containing a hole of the same diameter as the target was located parallel to the target about 1 cm away. This electrode could be biased to a few hundred volts positive which was sufficient to draw away electrons produced at the target.

3.3 Electron-Energy Spectrograph and Detector

3.3.1 Design Considerations

The design of the spectrograph for measurement of the energy spectrum of the emitted electrons was selected after consideration of time-of-flight, magnetic, trochoidal, and electrostatic analyzers. The type chosen was the parallel plate electrostatic spectrograph for low energy electrons (T. S. Green and G. A. Proca, Reference 17).

In this instrument, electrons enter a uniform retarding field at an angle of 30° to the equipotential planes, are deflected by the retarding field,

pass out through the entrance plane, and travel in a field-free region to the focal plane. The focal plane lies in the field-free region at an angle of 10.9° to the equipotential planes. This angle yields second order focusing by minimizing aberrations. The displacement along the focal plane is given by

$$x \text{ (cm)} = 5.29 [U \text{ (eV)}/2E \text{ (V/cm)} - h \text{ (cm)}] \quad (3.2)$$

where h is the distance from the source to the entrance plane. The energy dispersion is independent of electron energy

$$dU/dx \text{ (eV/cm)} = 0.379 E \text{ (V/cm)} . \quad (3.3)$$

The magnification of the analyzer is 1.5. A resolution of 0.5 eV with a minimum reasonable dispersion of 0.1 cm/eV yields an image 1.9 cm long for the desired energy range of 1 to 20 eV. The electric field implied by the required resolution is 26.4 V/cm or less. Such fields could be produced by a stack of guard plates (as in the Green and Proca design) and could be maintained uniform. Because the dispersion is independent of electron energy, electrons can be accelerated into the spectrograph without loss of resolution. It is also possible to "tune" the spectrograph for higher energy electrons, at the expense of resolution, by decreasing the accelerating potential.

In the final design of the spectrograph, the distance from the source to the analyzer h is chosen to be 2 cm. Then Eq. (3.2) establishes the minimum electron energy to be transmitted through the analyzer ($x = 0$) as 106 eV for a field E of 26.4 V/cm. This requires acceleration of electrons into the analyzer. The low energy end of the focal plane lies at $3\sqrt{3} h$ or 10.4 cm from the source, and the high energy end 1.9 cm further. The entrance slit subtends 12° and is 1.5 cm long. Assuming a focal plane width of 2 cm, one calculates that an entrance slit width of 0.3 cm is adequate to view the source. This provides a transverse angle of 9.3° . An electrode spacing of 3 cm is adequate to allow the trajectory of the extreme 36° ray to pass through the analyzer.

3.3.2 Detector Considerations

One of the simplest integrating detectors for electrons is photographic film. Direct photographic recording of electrons of 5 eV has been (Ref. 18) reported and recording of 50 keV electrons on film in vacuum for electron microscopy is routine. Electrons of a few kilovolts energy have a range of only a micron in silver bromide, so that practically only one grain layer on the film is affected, and films with supercoating layers of gelatin should be avoided. As an example of film sensitivity, Kodak Electron Image Plates when processed in (1:2) HRP developer have an electron speed of 2 for 50-100 keV electrons. This implies an exposure of 5×10^7 electrons/cm² to produce a density of 1.0 above gross fog. Because the total electron emission of the target is only 7×10^4 electrons, it is impossible to achieve integrated electron exposures of this size by accelerating the electrons emerging from the spectrograph directly into the film.

A high resolution, high sensitivity channel plate image intensifier for use in particle spectrographs (Reference 19) has been tested with the Green and Proca parallel plate electrostatic spectrograph. The electron energy spectrum, dispersed along the focal plane, is the electron image which is amplified by a channel plate multiplier. Additional gain might be achieved by acceleration of the electrons from the focal plane to the input of the channel plate multiplier. The electrons emerging from the multiplier are accelerated to several kilovolts into a thin aluminum film deposited on the face of a scintillator. The thin film has high electron transmission and provides a uniform accelerating field but excludes any light. The photons generated in the scintillator are coupled to a photographic plate by fiber optics. The fast time response of the scintillator is not required in these experiments, and it could be replaced by a fluorescent screen.

To assess the feasibility of the proposed combination of parallel plate analyzer and image intensifier we can calculate backwards, from detector to the laser target. To obtain a density of 0.6 above fog (25% transmission) on a typical spectral photographic plate (Ref. 20) requires 0.03 photons per square

micron. Because the image intensifier yields 10^5 photons per electron, the required input to the image intensifier (at the image plane of the analyzer) is 30 electrons per square cm. (Of course, statistical fluctuations alone would make analysis of such a small number of electrons impractical. This number is considered in order to examine a worst case situation. In actual experiments, as explained below, a substantially larger number of electrons will be analyzed.) The dimensions of the image are 2 cm by 2 cm, so that about 120 electrons must be transmitted by the analyzer. The acceptance angle of the spectrograph is 12° in the energy-dispersing direction. In the transverse direction the image of the $40\text{ }\mu\text{m}$ spot on the laser target is 2 cm wide at a maximum distance of 12.3 cm. The minimum transverse angle subtended is about 9.3° . If we make the stringent assumptions that the laser target emits electrons isotropically into the 2π solid angle and that the energy distribution of the electrons is flat over the energy range 1-20 eV (so that the electrons spread uniformly along the image plane), then the total number of electrons leaving the target would have to be about 2.5×10^4 . For a laser pulse of 200 ns duration this represents a current of 1.3×10^{11} electrons per second for an emitting point. Musal (Reference 3) calculates that a current of this size could be produced by laser flux densities of $50\text{--}500\text{ Mw/cm}^2$, depending on his choice of conditions. (For example, a field emission point one micron high with a field enhancement of 100 would emit 3.6×10^{11} electrons for a laser power density of 100 Mw/cm^2 , and a point of 0.3 microns with a field enhancement of 30 would emit 4×10^{11} electrons at 1 Gw/cm^2).

For several reasons the example just discussed is a worst case situation. First, the blackening of film to $D = 0.6$ is a severe requirement for plates to be read on a microdensitometer. Second, the energy spectrum of the electrons will not be flat but will peak at some energy of interest increasing the signal in the appropriate part of the image. Third, the electrons will probably not be emitted isotropically but will be preferentially accelerated along the direction of the electric vector of the laser radiation and into the spectrograph. Finally, not only does the emission per point rise

rapidly with increasing laser power density, but the number of emitting points has also been observed to increase. Because the calculation for these worst case assumptions indicated that the experiment was feasible with the proposed apparatus, it was reasonable to expect that the experiment could be successful under the actual conditions.

The channel plate image intensifier with photographic film recording was judged to be the most appropriate for use with the parallel plate electrostatic spectrograph.

A schematic diagram of the experimental arrangement as originally conceived is shown in Figure 3-2.

3.3.3 Hardware

The electron spectrograph has been designed, built and calibrated. The base plate is made from 0.1 inch thick stainless steel and the electrodes from 25 mil advance metal. The electrodes are 2 inches wide by 7 inches long with cutouts of 0.5 by 6.1 inches for the electron trajectories. The electrodes are supported from the base by 14 aluminum oxide rods and spacers located along the outside edges. A uniform electric field is produced by a voltage on the electrodes supplied through a voltage divider of precision glass-encapsulated resistors located within the vacuum system. The base plate contains both the entrance and exit apertures for the electrons. It is 8.85 inches long and is interfaced to the input plane of the detector at the required angle of 10.9° by means of a wedge-shaped, hollow, cylindrical support. The base plate bolts to this wedge which, in turn, is bolted to the flange containing the detector and the fiber optic output window. The Channetron^(R) Electron Multiplier Array (CEMA) constructed to our design by Galileo Electro-Optics has a 40 mm active diameter with 25 μ m pore size. The input to the fiber-optic window is vacuum sealed to a flange to carry the light of the output signal through the vacuum wall where the signal is recorded on film. Thus, the entire assembly-electron spectrograph, detector,

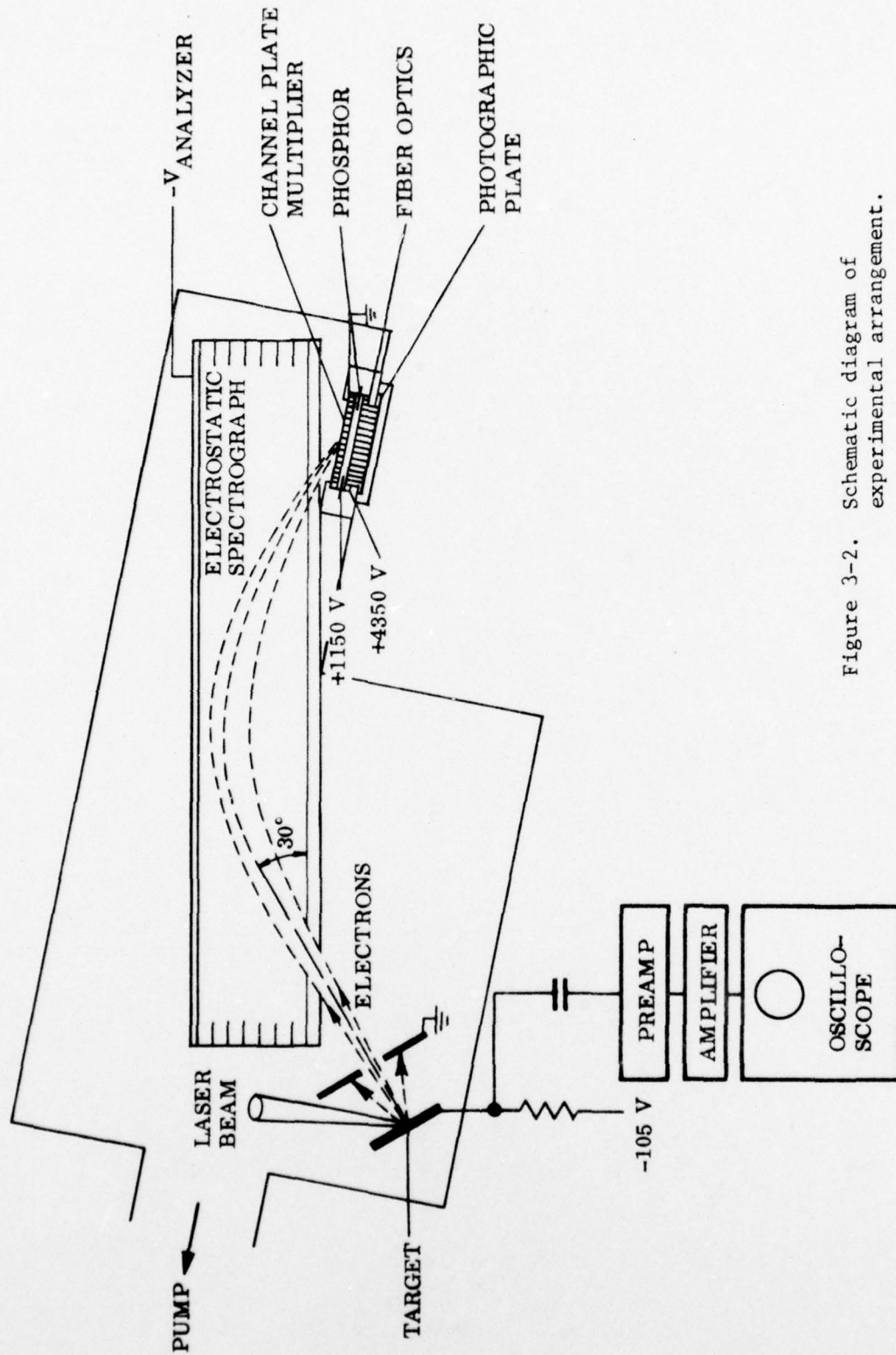


Figure 3-2. Schematic diagram of experimental arrangement.

and fiber-optic output is mounted on a single flange which can be assembled and aligned outside the target chamber and then fitted into the box-like "top-hat" on the lid of the target chamber. A scale diagram of this arrangement is shown in Figure 3-3.

3.3.4 Calibration

Calibration of the energy transmission and resolution characteristics of the system was accomplished by using a tungsten spiral-wound filament as an electron gun cathode which was located behind a pinhole. The cathode was biased to a negative voltage (shown as electron energy U) and the plate containing the pinhole was grounded. From Eq. (3.2) one expects the energy of electrons reaching a fixed point on the focal plane of the spectrograph to be linearly dependent on the analyzer field E

$$U \text{ (eV)} = E \text{ (V/cm)} \left[.379 x \text{ (cm)} + 2h \text{ (cm)} \right] \quad (3.4)$$

This is confirmed in Figure 3-4 which is a plot of the energy of electrons reaching the center of the CEMA output circle versus analyzer field. The design value of x to the center of the CEMA was 6.9 cm and with $h = 2.0$ cm, the design slope of the U versus E plot was calculated to be 6.61 to be compared with a measured value of 6.60.

The energy dispersion of the spectrograph as a function of analyzer field is shown in Figure 3-5. From the design equation (3.3) the plot is expected to be linear with a slope of 0.379. The observed plot is linear with a slope of 0.335, within 10% of the design value.

The energy calibration of the spectrograph is sensitive to the position h of the electron source (see Eq. 3.4). The value of h is difficult to ascertain directly because of the odd angles involved and because the target is mounted from the base of the chamber and the spectrograph is mounted on the lid. Consequently, an empirical in situ alignment and calibration is

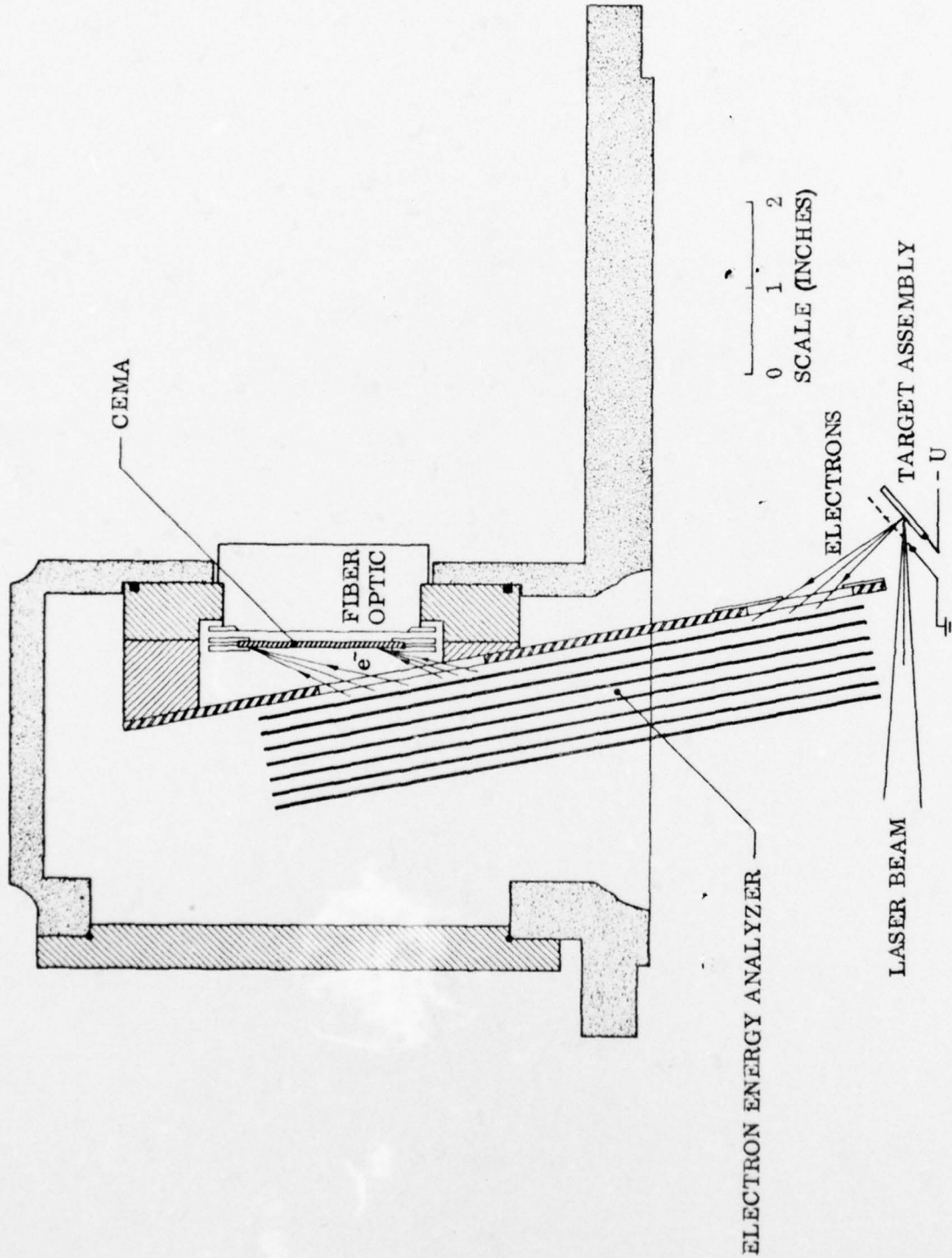


Fig. 3-3 Scale diagram of electron energy spectrograph and detector assembly in cross section through lid of target chamber.

LMSC-D566093

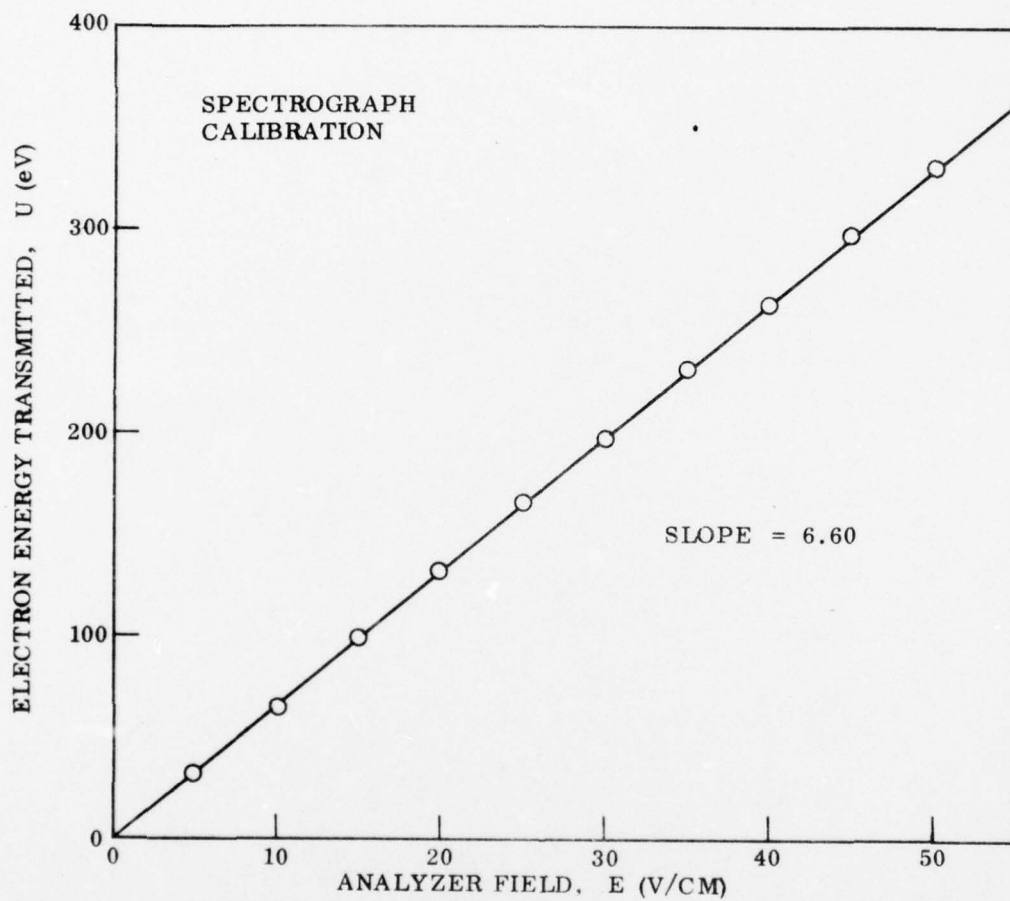


Fig. 3-4. Tuning of the Electron Energy Spectrograph. The energy of the electrons reaching the center of the CEMA shows a linear dependence on the retarding electric field of the analyzer.

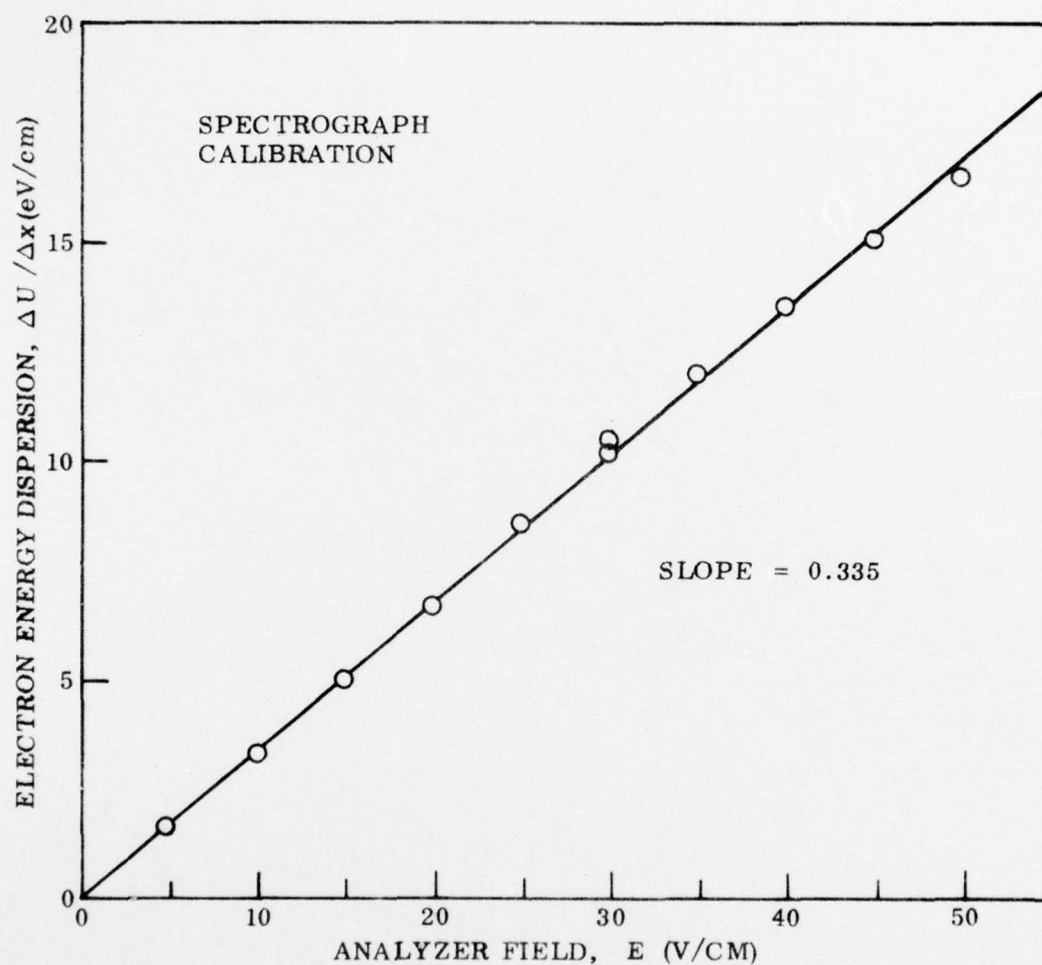


Fig. 3-5. Dispersion of the Electron Energy Spectrograph. The difference in electron energy required to strike the CEMA at points 1 cm apart is a linear function of the retarding electric field of the analyzer.

provided by placing an electron filament behind at pinhole at one side of the target assembly level with the target surface. The pinhole is visually located as close as possible to the best source location, and final adjustments to achieve the narrowest, brightest line at the output of the spectrograph are accomplished in vacuum using the electron source. The energy calibration is then established by the bias on the filament. The laser focus is then brought into registration with the pinhole by use of the visible alignment beam passing along the laser axis. Finally, the target is displaced sideways to bring the target material into testing position.

Photographs of the output were taken at $f/1.4$ on Polaroid Type 410 film with a camera of the type used for oscilloscope photos. Figure 3-6 is a multiple exposure photo with different bias voltages applied to the tungsten filament electron source. The horizontal slightly curved lines are produced because there is no focusing in the transverse direction by the spectrograph. A transparent millimeter grid was placed across the output face to aid in calibration.

3.3.5 Modification

When the analyzer was used with a laser shot, a large bright spot appeared on the screen at analyzing voltages corresponding to slightly less than the accelerating voltage from the target (Fig. 3-7). This effect probably results from electrons produced at the solid plate at the rear of the analyzer by photons coming from the target. These spurious electrons mask the desired signal of electrons emitted from the target. To reduce this undesired current, the rear analyzer plate was replaced by a high-transmission nickel grid to maintain the electrical characteristics of the analyzer while permitting the photons to pass out of the analyzer. Efforts on further development of the electron energy analyzer were concluded at this point because of termination of funding.

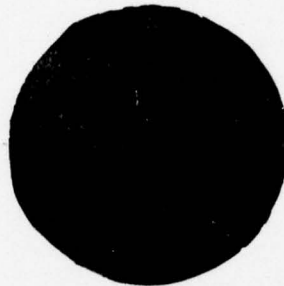


Fig. 3-6. Calibration of Electron Energy Spectrograph. Multiple exposure of electrons from filament and pinhole calibration source shows energies from 150 to 174 eV in 2 eV steps plus 155, 165, 175 eV. Analyzer field was set at 25 V/cm.



Fig. 3-7. Energy Spectrogram of Electron Distribution from Laser Pulse on Al Alloy Target showing spurious bright spot due to photoelectrons produced inside the analyzer.

3.4 CO₂ 10.6 μ m Laser

3.4.1 Experimental Apparatus

Laser pulses of 0.3 microseconds duration at 10.6 μ m wavelength were obtained by mechanically Q-switching a Coherent Radiation Model 43 CO₂ laser. The laser has a 13 meter cavity and can produce 500 watts cw. To Q-switch the laser, the totally reflecting rear mirror was replaced by a pair of concave spherical mirrors which are adjusted to reproduce the focal length of the rear mirror. A small focal spot is created between the concave mirrors, and the laser beam path is chopped at this point to produce Q-switching. Beam chopping is produced by transmission through a 10 mil slit in a 3.25 inch diameter Al wheel which was dynamically balanced and driven at 400 Hz by a synchronous motor. Because the chopper is mounted on the laser end plate, it reaches a 20 kV potential during the striking of the discharge. The chopper motor power supply is isolated by a high voltage transformer.

The optics and chopper motor are water-cooled and all are located within the vacuum system of the laser; that is, they are immersed in the CO₂-N₂-He gas medium. Excited species from the discharge are free to migrate into the Q-switch assembly and probably were the cause of turning the black-anodized chopper wheel to a golden color. The water cooling connections among the copper heat-sink mounts were originally made by rubber surgical tubing. Unfortunately, stray reflections of the laser beam during adjustment of the chopper wheel burned holes in the tubing admitting cooling water to the laser cavity. Satisfactory results were achieved by use of flexible stainless steel tubing and compression fittings for the water cooling system.

Because individual submicrosecond pulses were required for these experiments, a chopper wheel containing a single transmitting slit was tried. From the 400 Q-switched pulses per second produced by this arrangement, a single pulse was isolated externally to the laser by a solenoid-driven shutter which remained open for 2.5 milliseconds. Although this method

yielded the desired pulse, it also resulted in a large number of noise pulses and severe erosion to the chopper wheel. Much more energy was contained in the sum of the noise pulses than in the main Q-switched pulse. Observations showed no noise pulses for a short time after the main Q-switched pulse and little erosion on the area of the chopper wheel which immediately followed the slit into the beam. Evidently, the time required for the continuous discharge to create a population inversion in the lasing medium is short compared to the 2.5 ms between Q-switched pulses, and there is sufficient gain in the laser medium to cause the laser to fire on spurious reflections from the chopper wheel.

Relatively clean Q-switched pulses were obtained by chopping at a faster rate. A chopper wheel containing 12 equally spaced slits was run at 400 Hz to yield 4800 pulses per second, that is, a pulse spacing of 208 microseconds. Although spurious pulses were not completely eliminated, both their size and frequency were markedly reduced to five or less noise pulses per Q-switched pulse with a total energy content always less than half that of the main pulse and usually much less. Figure 3-8 shows the experimental setup.

To isolate a single Q-switched pulse from the pulse stream, a rotating shutter wheel was placed external to the laser in series with the solenoid driven shutter. This wheel contained six 3/8 inch diameter holes spaced on a 7.50 inch diameter circle. The wheel was driven by a variable speed ac motor at about 4800 rpm to provide a clear aperture for 200 μ s spaced about 2 milliseconds apart. The speed of the solenoid driven shutter was increased so that it remained open for 2 milliseconds. The "open" status of each shutter was monitored by a light source coupled to a phototransistor. The triggering of the single-shot solenoid-driven shutter could be adjusted through a time delay circuit and observed on an oscilloscope. The timing was set so that the 200 μ s "open" time of the shutter wheel fell at the middle of the 2 ms "open" time of the single-shot shutter. Because the Q-switched laser pulses were spaced about 200 μ s apart, this arrangement insured transmission of a single Q-switched pulse for each firing of the solenoid-driven shutter.

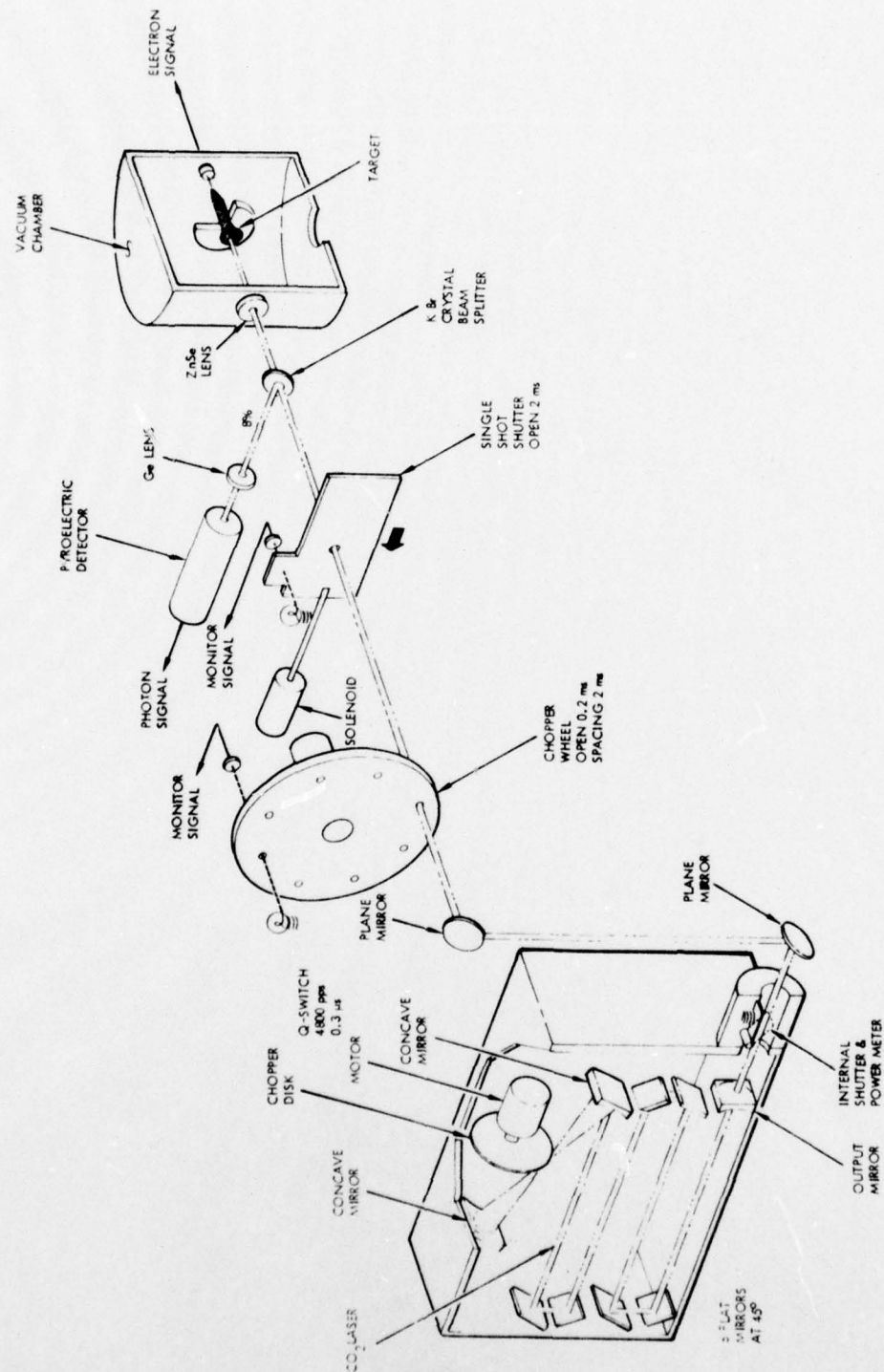


Figure 3-8. Schematic diagram of experimental arrangement for experiments with Q-switched pulses from the CO₂ laser.

The internal safety shutter on the laser housing was used to block the laser output except for a few seconds during a shot.

A manually operated beam flag was placed between the exit of the discharge tube and the first spherical mirror of the Q-switch chopper. The flag was removed from the beam path only when laser shots were being made. This device permitted the discharge to be run continuously, thus enhancing the stability of the laser while preventing the beam from reaching the mirror being focused to a spot and eroding the chopper wheel.

The beam exit from the laser was located only a few inches from the floor. The beam was raised to the height of the target chamber by a periscope arrangement of two front surface Al mirrors. The lower mirror deflected the beam vertically and changed the beam polarization from horizontal to vertical. The upper mirror deflected the beam to the horizontal and at right angles to the original direction of the beam emerging from the laser. The beam polarization remained vertical after this reflection.

The laser beam then passed through the shutter wheel, and the single shot shutter. A KBr crystal plate beam splitter located in front of the target chamber reflected about 8 percent of the beam into a beam monitor. The main part of the laser beam passed on to the 2.5 inch focal length ZnSe lens sealed into the target chamber and was focused onto the target.

The beam monitor consisted of a 1.5 inch focal length Ge lens and a Molelectron P3-00 pyroelectric detector. To obtain 10 mV signals to display directly on the oscilloscope a feedback resistor of 510 K was used which made the detector risetime 250 nanoseconds. The beam monitor response was calibrated against a small, precalibrated tantalum foil calorimeter, using single pulses from the laser. The reflectance of the anodized Ta foil was measured independently ($R = 0.86$), and a linear calibration was obtained between the voltage output of the pyroelectric detector and the energy delivered to the target.

During an experiment the signal from the pyroelectric detector was fed into one channel of a Tektronix Type 551 dual beam oscilloscope (main-frame risetime 12 nanoseconds) with Type 53/54B wideband calibrated preamp (risetime 25 nanoseconds).

The laser-induced electron emission was measured as electron current leaving the target. Two AvanteK Type AV-9T solid state amplifiers with 0.7 nanosecond risetimes and voltage gains of 32.5 and 35.5 were used to amplify the electron signal which was fed into the other channel of the dual beam oscilloscope through a Type 53/54K fast rise calibrated preamplifier (risetime 6 nanoseconds).

A thin metal plate containing a hole for passage of the laser beam was placed 1 cm from the target. A dc voltage could be applied to this plate to produce a drawout field for the electrons emitted from the target.

The oscilloscope was triggered by a signal derived from the shutter monitors through an Ortec Type 418 coincidence unit which fired when both the solenoid shutter and the rotating shutter were open. A sweep speed of 20 micro-seconds/cm was used to display the entire period when the shutters were open. A faster sweep speed based on internal triggering derived from the laser signal was found to be unsatisfactory. The scope tended to trigger on small noise pulses from the laser, and the fast sweep speed would cause the main peak to be missed. Internal triggering on the electron signal was successfully accomplished for one set of runs so that a faster sweep speed could be used and the temporal structure of the laser and electron pulses could be observed. This mode of operation was not satisfactory for monitoring every shot because electron pulses were not always obtained, and in this event this scope would not trigger and no record of the laser pulse for diagnostic purposes could be obtained. Ideally, two double beam scopes should be used, one at slow sweep speed to give a complete record of each shot and one at fast sweep speed to record the temporal structure of the pulse. Unfortunately, two dual beam scopes were not available for these measurements.

The pulses were photographed on Polaroid Type 410 film.

3.4.2 CO₂ 10.6 μ m Laser, Experimental Parameters

Determination of the laser irradiance onto the target requires measurement of the energy in the laser pulse, the pulse width, and the spot size.

The energy per pulse was determined by calibration of the pyroelectric detector against the tantalum foil calorimeter which had an output of 7×10^{-2} V/j. For this calibration the target was replaced by the calorimeter, and the calorimeter output was measured on a microvoltmeter. Multiplying the output of the pyroelectric detector used as a monitor in the split-off beam by 2.30×10^{-2} j/V yields the incident energy on target.

The area of the laser focal spot was determined by driving a knife edge through the beam. For this measurement, both shutters were left open and a continuous stream of pulses was delivered to a power meter downstream from the knife edge. The beam profile appeared nearly gaussian with a $1/e^2$ target spot area of 6.2×10^{-4} cm². The depth of focus was about 1 mm.

The full width at half height of the laser pulse averaged from 20 shots was 0.30 ± 0.04 μ s so that for a temporally gaussian pulse, the $1/e$ scale time is $0.30 \mu\text{s} / (2\sqrt{\ln 2}) = 0.18 \mu\text{s}$.

Assuming the pulse to be both spatially (x,y) and temporally (t) gaussian (Reference 21), one has the equation

$$I(x,y,t) = I_p \exp \left[-(2/w^2)(x^2 + y^2) \right] \exp (-t^2/\tau^2) \quad (3.5)$$

where I is the irradiance, I_p is the peak irradiance, w is the beam radius, and τ is the $1/e$ scale time. The total energy in a pulse E_t is

given by integration

$$E_t = \int_{-\infty}^{\infty} \int_{-\infty}^{\infty} \int_{-\infty}^{\infty} I(x, y, t) dx dy dt \quad (3.6)$$

$$E_t = 1/2 \pi^{3/2} w^2 \tau I_p \quad (3.7)$$

Solving for the peak irradiance, one obtains

$$I_p = \frac{2 E_t}{(\pi w^2)(\sqrt{\pi} \tau)} \quad (3.8)$$

where πw^2 is the $1/e^2$ target spot area.

Inserting the measured parameters, one obtains the calibration equation relating the photon irradiance in this system to the total energy in the laser pulse

$$I_p = 1.01 \times 10^{10} w \text{ cm}^{-2} \text{ j}^{-1} E_t \quad (3.9)$$

The electron current density is obtained from the peak value of the oscilloscope signal and the effective emitting area. As noted earlier, the electron signal was amplified through two fast pulse amplifiers having characteristic input and output impedances of 50 Ω and into a 50 Ω terminator on the oscilloscope.

The peak electron density J_p was obtained from

$$J_p = \frac{V_p}{A_1 A_2 50 \Omega (\pi w^2)} = (2.80 \times 10^{-2} \text{ A cm}^{-2} \text{ V}^{-1}) V_p \quad (3.10)$$

where V_p is the peak voltage deflection on the oscilloscope, $A_1 A_2$ are the gains of the amplifiers, and πw^2 is the $1/e^2$ area of the laser spot, which was taken as the effective area for electron emission.

3.5 1.06 μ m Laser Pulse Characteristics

The data at 1.06 μ m were obtained with single pulses selected from a Q-switched, mode-locked train from an Nd:glass laser and passed through two isolators located within four stages of amplification. The experiments were run concurrently with another study which required higher irradiance. To do this approximately 10% of the beam was split out with a pellicle located just upstream from the fifth amplifier, and a mirror was used to reflect this weaker beam into the target chamber built for this experiment. Neutral density filters located in front of the focusing lens for the target attenuated the laser beam by factors of about 10^{-5} to 10^{-3} to cover the desired range of irradiance (10^6 to 10^8 w/cm²). The pulse length of the laser was measured as 125 ± 25 ps by a streak camera, where the limits include the pulse-to-pulse variations. The area of the target spot was taken as the area of the circular white spot (about 1.5 mm in diameter) produced on blackened polaroid print by an unattenuated, focused laser pulse. The average area was 1.84 ± 0.02 mm².

The energy in each pulse was obtained from a calorimetric monitor of the main laser beam which in turn was calibrated against a calorimeter placed in the beam split-off for the experiments reported herein. The energy per pulse for these experiments ranged up to 0.2 J before attenuation.

The laser beam entering the target chamber was elliptically polarized with the major axis at about 4:30 o'clock (looking into the target).

For measurement of the polarization dependence of electron emission, the fast response target described above was rotated 45° about a vertical axis, and the drawout electrode was shifted slightly to give an unobstructed view of the target from the lens. A polarizer was oriented along the major axis of the ellipse of polarization of the laser beam (45° ccw from the vertical) to assure linear polarization at the target. This was followed by a half-wave plate which was set with its principal axis at an angular displacement

of 22.5° to either side of the direction of polarization. Setting the axis of the half-wave plate between the incident polarization and the vertical rotated the polarization direction to vertical, and the polarization vector of the beam striking the target fell along the target surface. Setting the axis of the half-wave plate between the incident polarization and the horizontal rotated the polarization direction to horizontal, and the polarization vector of the beam striking the target had a large component perpendicular to the target surface.

The incident irradiance was computed from the measured energy, known pulse width, and the area of the elliptical white spot produced on a blackened polaroid print by an unattenuated, focused laser pulse (3.90 mm^2). Because the half-wave plate had an effective diameter of only 0.5 inch (compared with an 0.875 inch diameter of the laser beam), the area of the smaller elliptical spot produced by the laser beam after passing through the collimator for the half-wave plate was used to calculate the electron current density (0.99 mm^2).

3.6 Target Materials

The targets which were studied are discussed below.

A high purity ($> 99.9\%$) aluminum sample was chemically etched and cleaned in distilled water to provide a flat metal surface free of impurities. To provide a roughened surface another sample of high purity aluminum was abraded with "Scotchbrite" abrasive pad and then ultrasonically cleaned to remove traces of abrasive.

A cast aluminum sample provides a metal surface containing a relatively large concentration of absorptive inclusions.

Two samples of commercial rolled aluminum plates were used in "as received" condition after washing with detergent, distilled water, and alcohol to remove surface contamination. Aluminum 6061-T6 has the composition

0.25 percent Cu, 0.6 percent Si, 1.0 percent Mg, 0.25 percent Cr, balance Al; and aluminum 2024-T3 has the composition 4.5 percent Cu, 0.6 percent Mn, 1.5 percent Mg, balance Al (Reference 22). In addition, the surface of one sample of Al 6061-T6 was roughened with "Scotchbrite" abrasive pad to provide an abraded surface for study.

A type of target containing a large number of field emission points was purchased from SRI. It consists of a regular array of microscopic cones on 1 mil centers produced by vacuum evaporation of copper through a screen onto a molybdenum substrate. As deposition proceeded, the holes in the screen filled up, less vapor was transmitted, and a regular square array of field emission points was produced. The cones were then overcoated with aluminum.

Type 321 stainless steel was used in "as received" condition after rinsing with alcohol. The principal alloying elements are 18 percent Cr, 13 percent Ni, and traces of Ti (Reference 22).

Titanium alloy was used in "as received" condition after rinsing with detergent, distilled water, and alcohol. Composition of Ti-6Al-4V alloy is 5.50-6.75 percent Al, 3.50-4.50 percent V, less than 0.5 percent of any other impurity, and balance Ti (Reference 22).

Thin sheets of high purity gold and silver were cleaned and fastened to aluminum disc substrates with conductive epoxy adhesive.

A sample of practical material was provided by the Air Force Materials Laboratory. It consisted of an aluminum disc treated with bright dip, alodined, coated with cleanly degrading polymer, and painted with yellow primer.

Section 4

RESULTS AND DISCUSSION

The results of the application of the experimental procedures described in the preceding section to the materials described therein are reported and discussed in this section.

First, experiments at 10.6 μm using the CO_2 laser are considered for targets of stainless steel, titanium alloy, aluminum materials prepared in different ways, and other materials. Next experiments at 1.06 μm using the Nd laser are reported, in particular, the time dependence of electron emission, the effect of polarization of the laser beam, and the peak emission current of electrons as a function of laser irradiance for several different materials. Finally, the implications of these results are discussed.

4.1 Experiments at 10.6 μm

The maximum irradiance obtained using the CO_2 mechanically Q-switched laser was about $1 \times 10^7 \text{ w cm}^{-2}$ in a pulse of 0.30 μs full width at half height. A detailed description of the laser pulse parameters appears in Section 3.4.3. The pulses occurred in a distribution of sizes and could not be preselected. Considerable scatter was obtained in all the measurements of electron emission. Relatively small electron pulses were sometimes associated with large laser pulses which usually produced large electron pulses. (Similar results have been observed by other workers, Reference 23). Microscopic variations in surface conditions undoubtedly account for part of the observed variation, but a more stable and reproducible laser pulse appears essential to future detailed studies.

4.1.1 Stainless Steel

The available laser irradiances span the LSDW threshold region for stainless steel. Figure 4-1 shows the dependence of electron emission on incident laser irradiance for "as received" Type 321 stainless steel. The points represent the largest values of peak electron emission current density observed at the given irradiances. The voltage on the drawout electrode was varied between 0 and + 500 V. Electron emission was observed at 0 V drawout in contrast to the behavior at 1.06 μm where no electron emission was observed with 0 drawout. Increasing the drawout voltage from 0 to 500 V tended to increase the size of the electron emission by roughly a factor of 3, but the scatter in the data was too large to permit establishment of quantitative relationship between drawout voltage and electron emission at fixed irradiance.

In Figure 4-1 the open circles correspond to data taken with the laser beam incident normal to the target. The crosses are data taken with the laser beam incident at 45° to the target; for these points the effective area for calculating both irradiance and current density was increased by $\sqrt{2}$ to account for the elliptical target spot. The polarization of the laser beam was in the plane of the target for both target orientations. The results from both orientations appear to cluster about a single, common curve.

It is noteworthy that no sharp break in electron emission appears at the threshold irradiance reported for initiation of LSD waves. Instead, the data on the log-log plot can be approximated by a straight line with a slope of about 3/4.

4.1.2 Titanium Alloy

The laser irradiances span the LSDW threshold region for Ti-6Al-4V alloy. Figure 4-2 shows the dependence of electron emission on incident laser irradiance for "as received" Ti-6Al-4V alloy. The points represent the

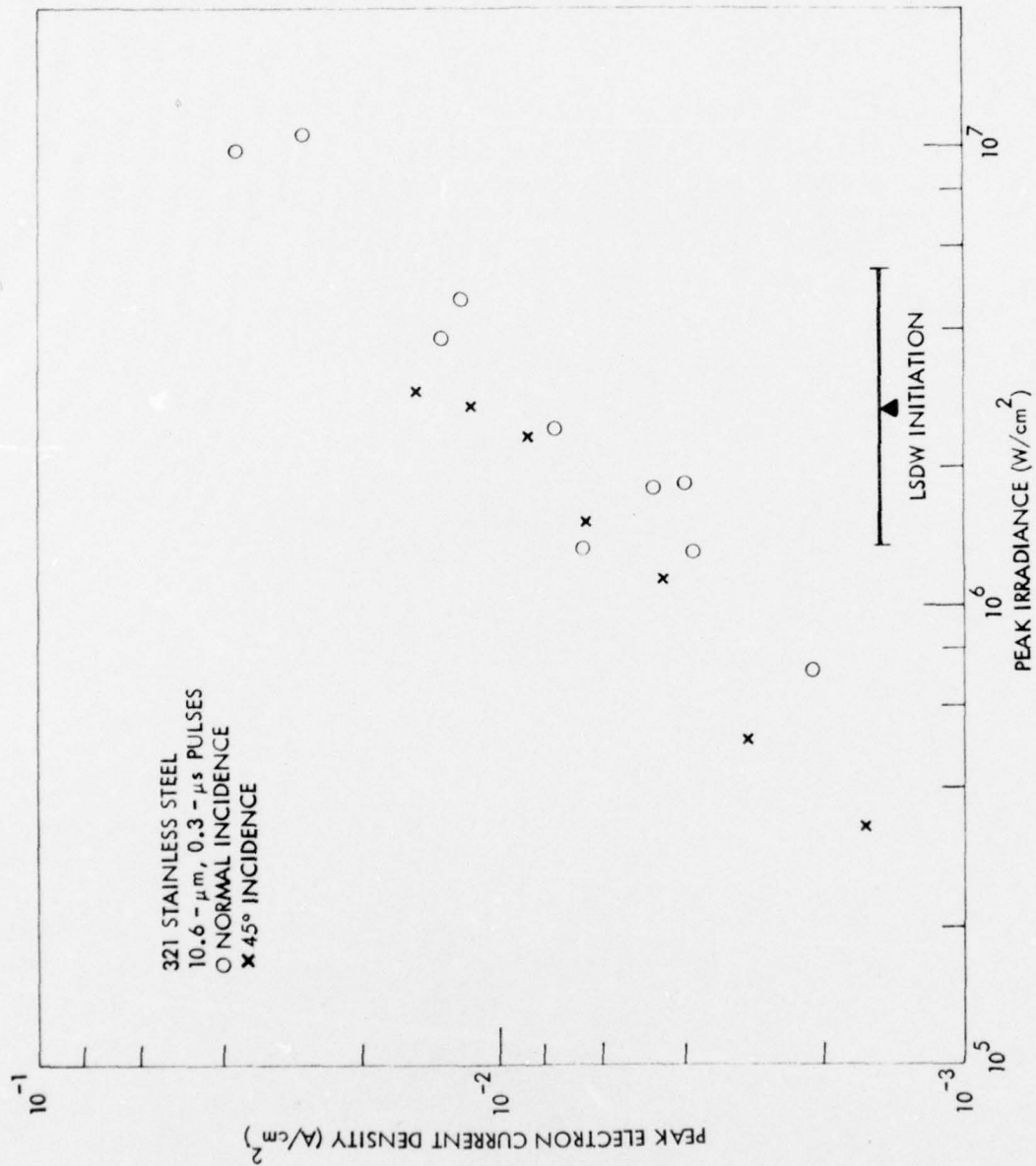


Figure 4-1. Dependence of Electron Emission from Type 321 Stainless Steel on Laser Irradiance at 10.6 μ m.

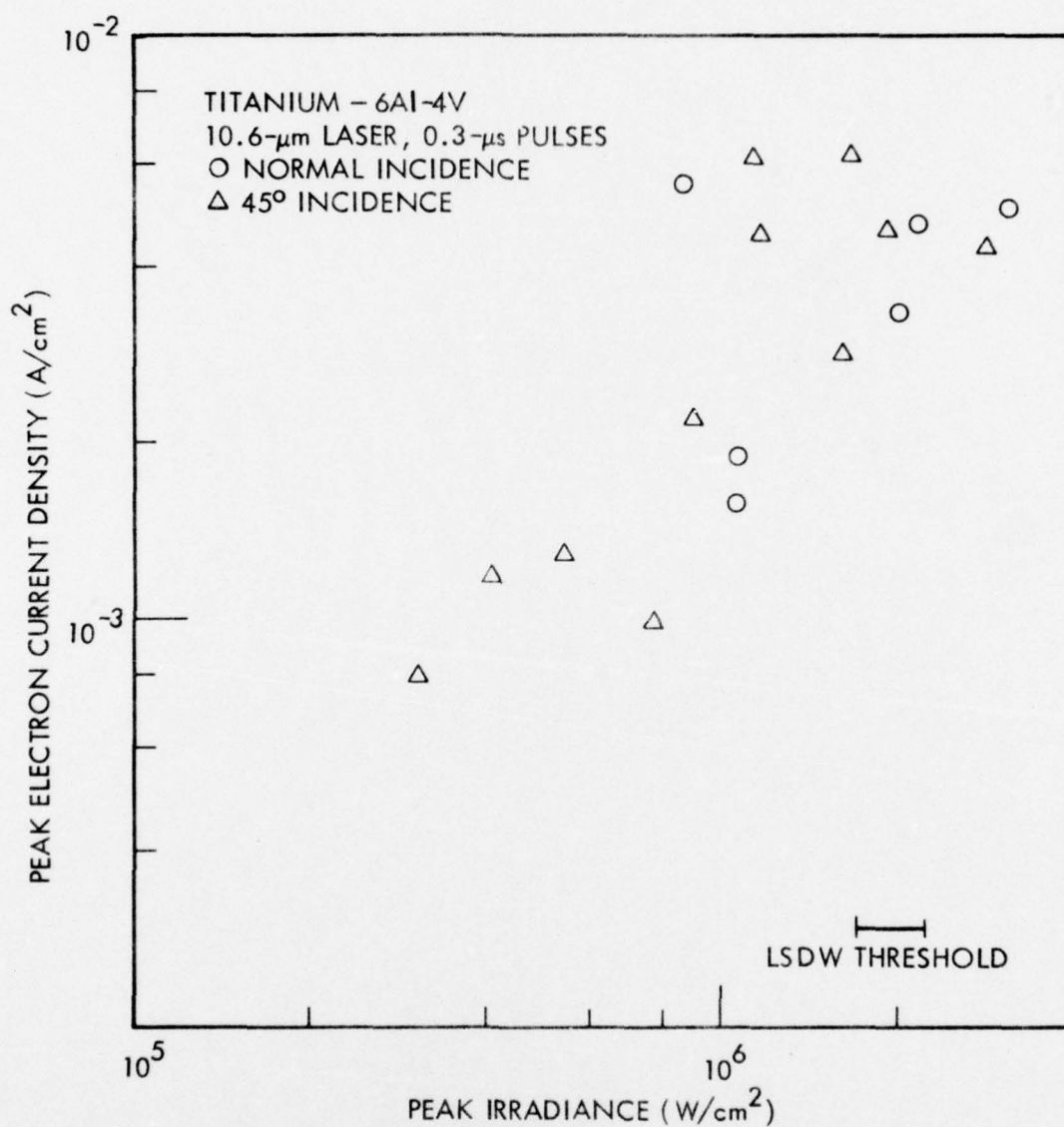


Figure 4-2. Dependence of Electron Emission from Titanium Alloy on Laser Irradiance at 10.6 μ m.

largest values of peak electron emission current density observed at the given irradiances. The voltage on the drawout electrode was varied between 0 and + 500 V. Electron emission was observed at 0 V drawout, but the scatter in the data was too large to permit establishment of a quantitative relationship between drawout voltage and electron emission at fixed irradiance.

In Figure 4-2 the open circles correspond to data taken with the laser beam incident normal to the target. The triangles are data taken with the laser beam incident at 45° to the target with the effective spot area increased by $\sqrt{2}$. The polarization of the laser beam was in the plane of the target. Although the scatter is large, the points from both target orientations appear to cluster together.

No sharp increase in electron emission appears at the threshold irradiance reported for the initiation of LSD waves. The data on the log-log plot exhibits a slope of approximately 2.

4.1.3 Aluminum-Containing Materials

Both the pure aluminum with the chemically polished surface and the 6061-T6 aluminum alloy were irradiated repeatedly and on different days at $10.6 \mu\text{m}$ with irradiances up to 10^7 w cm^{-2} without production of measurable electron emission. The lower limit of detectability of electron emission current density with this system is $8 \times 10^{-5} \text{ A cm}^{-2}$.

The surface of the pure aluminum sample was abraded with Scotchbrite and ultrasonically cleaned. Irradiation of this surface produced considerable electron emission. An irradiance of $6 \times 10^5 \text{ watt cm}^{-2}$ produced an electron current density of $4 \times 10^{-3} \text{ ampere cm}^{-2}$; $1.6 \times 10^6 \text{ watt cm}^{-2}$ produced $1.2 \times 10^{-2} \text{ ampere cm}^{-2}$. The large increase in electron emission resulting from roughening the aluminum surface is paralleled by the well-known observations of a reduction in the threshold irradiance requirement for LSD wave production when abraded surfaces are substituted for smooth ones.

Irradiation of the multipoint target array of aluminum overcoated copper micro-cones on a molybdenum substrate produced large electron currents. The initial laser pulse of 8×10^5 watt cm^{-2} produced an electron emission which went off scale, in excess of 10^{-2} ampere cm^{-2} . The second pulse at the same spot, 1.7×10^6 watt/ cm^{-2} , produced electron emission of 9×10^{-3} ampere cm^{-2} . Repeated laser pulses were directed on the same spot. The fifth pulse of 5×10^5 watt cm^{-2} produced electron emission of 0.11 A cm^{-2} . At the end of the sequence of seven laser shots at the same spot on the target, visual examination showed a small discolored pinhole area on the target array. Figures 4-3a and 4-3b show scanning electron microscope photos of the target area. The cones directly under the laser focus are missing; surrounding cones are distorted, and the aluminum overcoating is flaking on nearby cones. Microglobules of metal can be seen near the corners of the photo taken at lower magnification. Possible causes of the localized destruction of the multipoint array are ohmic heating from the electron flow or direct laser heating and melting.

4.1.4 Other Materials

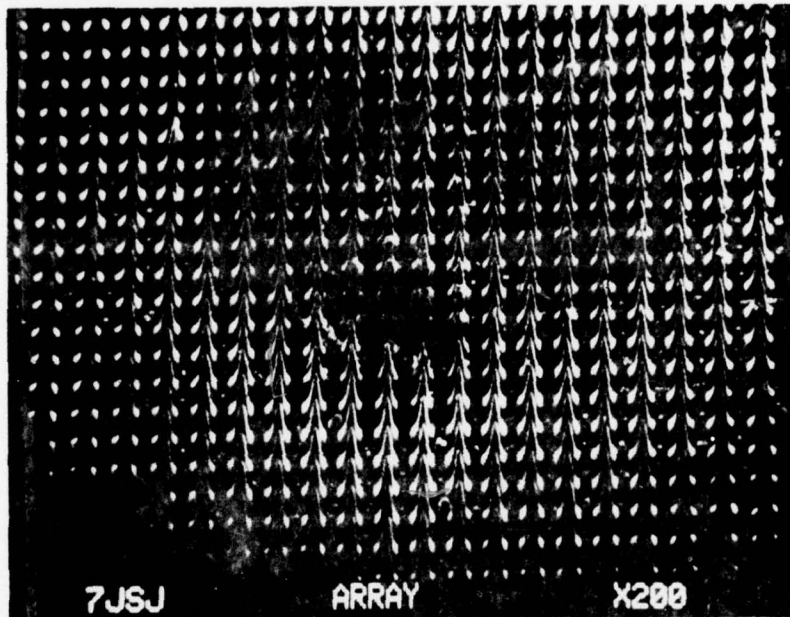
At the maximum laser irradiance obtainable from this system, typically $5 \times 10^6 \text{ w cm}^{-2}$, the electron emission was too small to be measured (less than $8 \times 10^{-5} \text{ A cm}^{-2}$) for gold, silver, cast aluminum, and the painted aluminum targets used in these experiments.

4.2 Experiments at $1.06 \mu\text{m}$

The range of irradiances from the Nd laser system used in these experiments was about 5×10^6 to 2×10^9 watt/ cm^{-2} in short pulse approximately 0.125 ns wide. The size of the pulses could be roughly preselected by adjusting the gains in the amplifier train. A detailed description of the laser pulse characteristics is given in Section 3.5.

To register a voltage signal at the scope from the electrons ejected by a laser pulse on the target it was necessary to create a small drawout

a.



b.

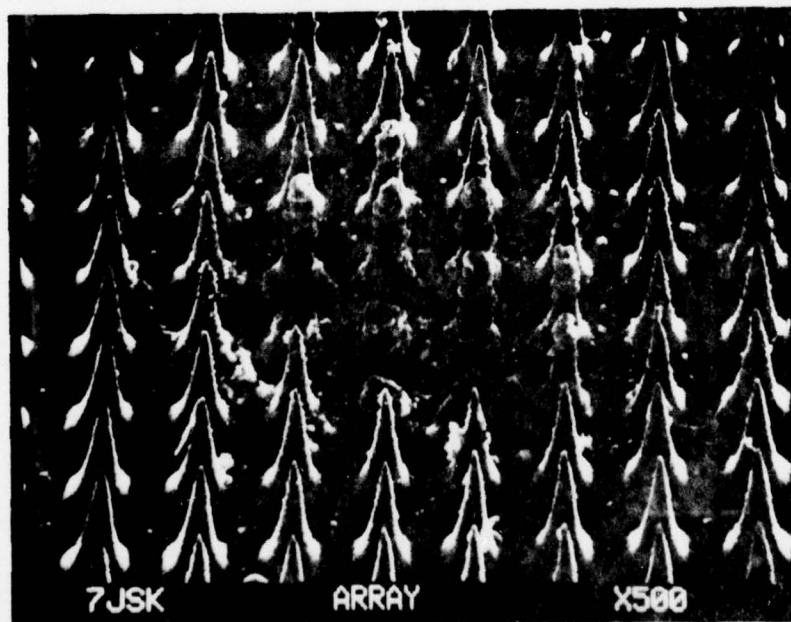


Figure 4.3. Scanning Electron Micrographs of Multipoint Array Irradiated 10.6 μm . a. 200X b. 500X. Points are aluminum overcoated on copper deposited on molybdenum substrate on 1 mil centers.

(of the order of 10 V/cm) field at the target face. A planar electrode containing a hole of the same diameter as the target was located parallel to the target about 1 cm away. Biasing this electrode to a few hundred volts positive was sufficient to develop the electron signal. Repeated checks showed that the signal disappeared when the bias was removed. This behavior contrasts with the behavior observed at 10.6 μm with longer pulses, both by Walters, (C. T. Walters, private communication) and herein where large signals from photoemitted electrons were obtained without the use of a drawout field.

4.2.1 Time Dependence of Electron Emission

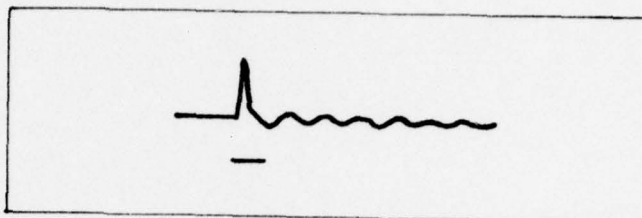
The time-dependence of the electron current pulses were found to vary with increasing irradiance in the short laser pulse. As shown in Figure 4-4a, for relatively low irradiance, the electron pulse is a sharp spike. As the irradiance is increased, a tail with a longer time constant appears on the trailing edge of the pulse (Figure 4-4b). At the highest power densities studied the initial spike completely disappears, and both a slower rise and long decay occur (Figure 4-4c). These results suggest the dominant electron-emitting process shifts from a prompt emission mechanism (for example, enhanced field emission) to a delayed emission mechanism (for example, thermionic emission) with increasing irradiance. Similar behavior was observed for all materials irradiated at 1.06 μm .

4.2.2 Polarization Dependence of Electron Emission

The results of the polarization measurements on 6061-T6 Al alloy are shown in Figure 4-5. Because substantially more electrons are emitted when the polarization vector points out of the target than when it lies in the target plane, it is clear that the electron emission process is strongly influenced by the electric vector of the laser light as would be expected, for example, for an enhanced field emission mechanism but not for a purely thermal effect.

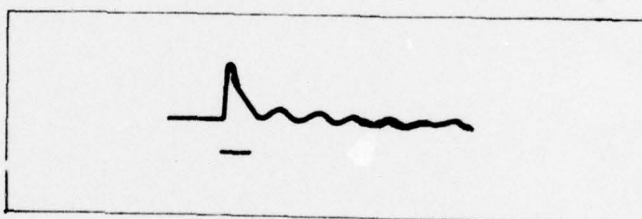
Electron emission from cast aluminum, however, is independent of the angle of polarization as shown in Figure 4-6. A mechanism which is independent

a. 20 mV/div



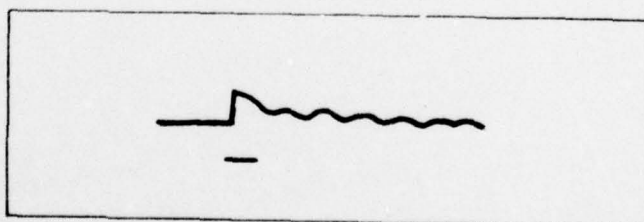
10 ns/div $G_p = 30 \text{ MW/cm}^2$

b. 50 mV/div



10 ns/div $G_p = 160 \text{ MW/cm}^2$

c. 100 mV/div



10 ns/div $G_p = 290 \text{ MW/cm}^2$

Figure 4-4. Oscilloscope Traces of Total Electron Emission versus Time at Different Laser Irradiances ($1.06 \mu\text{m}$, 0.1 ns pulses).

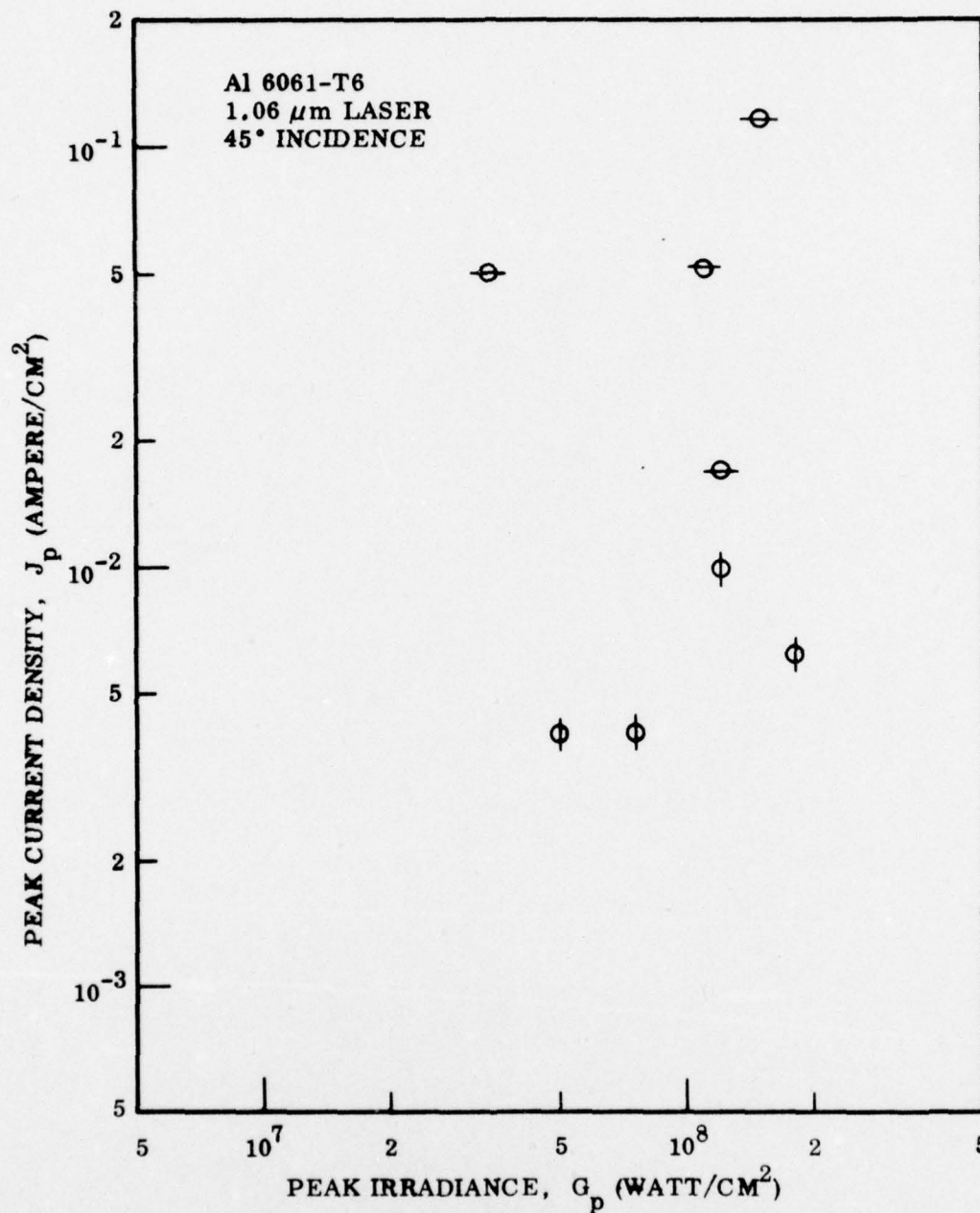


Fig. 4-5. Polarization Effect on Electron Emission. The direction of polarization of the laser radiation was parallel to the target plane for data points marked with vertical lines and perpendicular to the target plane for points with horizontal lines. The perpendicular orientation yielded greater electron emission.

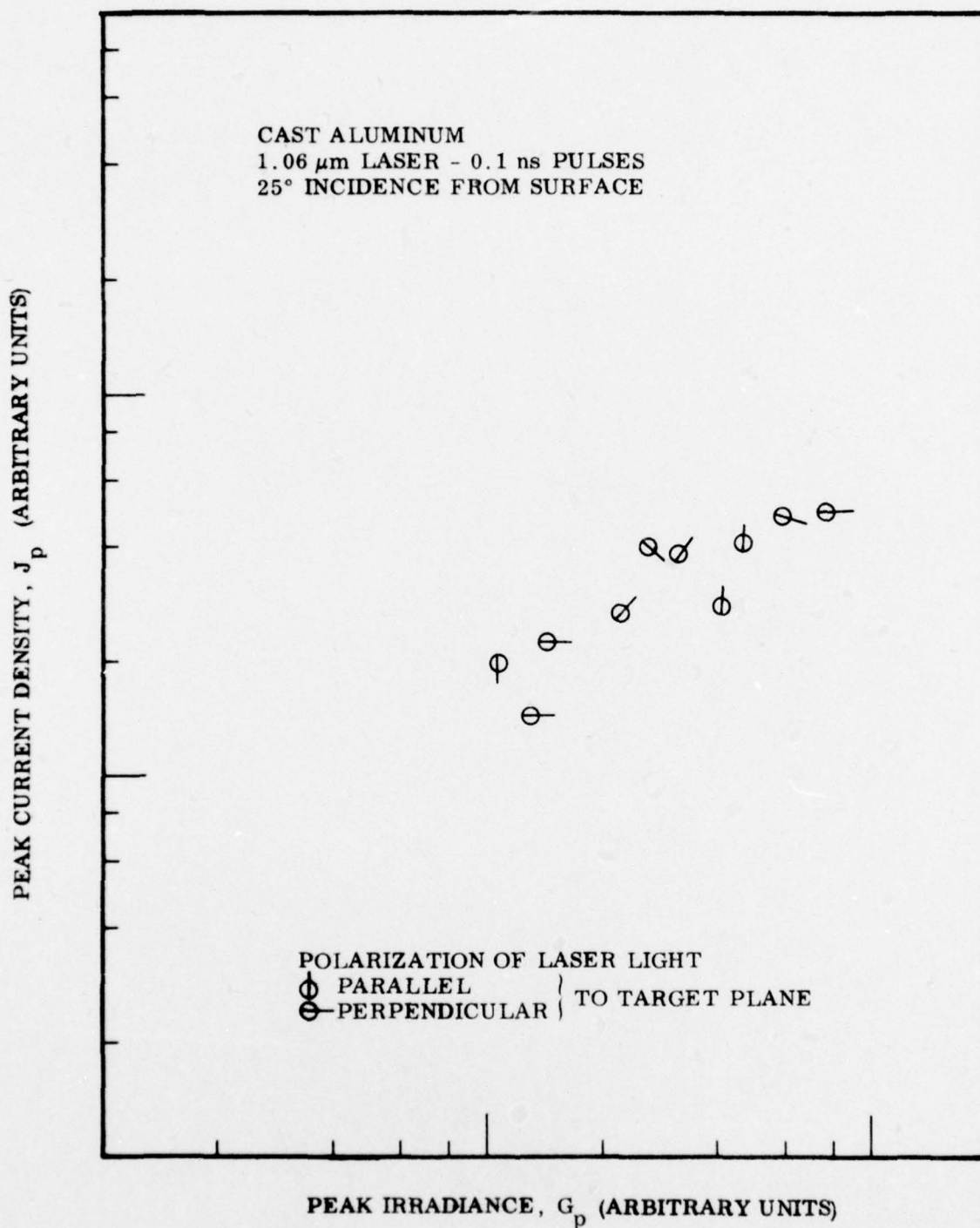


Fig. 4-6. Polarization Effect on Electron Emission. Target was cast aluminum. Emission of electrons is independent of direction of polarization of laser light.

of the direction of the electric vector of the laser light is dominant for cast aluminum, or the surface microstructure of cast aluminum is so rough that a variety of angles is presented to an incoming beam, obscuring the polarization effect.

4.2.3 Total Emission Studies on Various Materials

Plots of the peak electron current density J_p emitted as a function of laser irradiance for normal incidence of the laser beam on several targets are shown in Figures 4-7 to 4-9. The value of J_p was obtained by dividing the maximum voltage observed on the scope photograph by the 50 ohm scope termination and the area of the target spot. A new target spot was used for each laser pulse to avoid possible effects of annealing on a previous shot. A steady increase of electron emission with irradiance is observed, although there is appreciable scatter in the data. Note that the figures underemphasize the total emission of electrons at the higher irradiances because the long tail of the electron emission curve is not reflected in the plot of peak electron current density.

In Figure 4-7 the electron emission of cast aluminum a surface containing a relatively large amount of absorptive inclusions is given together with that for high purity, chemically etched aluminum. Comparison of the data shows no significant difference in electron emission between the two materials, except possibly at the lowest irradiance studied. For these tenth-nanosecond pulses at $1.06 \mu\text{m}$, the vaporization of volatile impurities does not appear to contribute significantly to the electron emission.

In Figure 4-8 is shown the electron emission from two different surface preparations of Al 6061-T6 alloy - "as received" and abraded. The abraded surface yields about twice the current density compared to the "as received" surface indicating the enhancement effect of surface irregularities. Comparison with Figure 3-3 shows that the current density emitted by the "as received" Al 6061-T6 alloy is two to three times that of the high purity, flat aluminum. It is not clear whether this difference is due to the rolling and

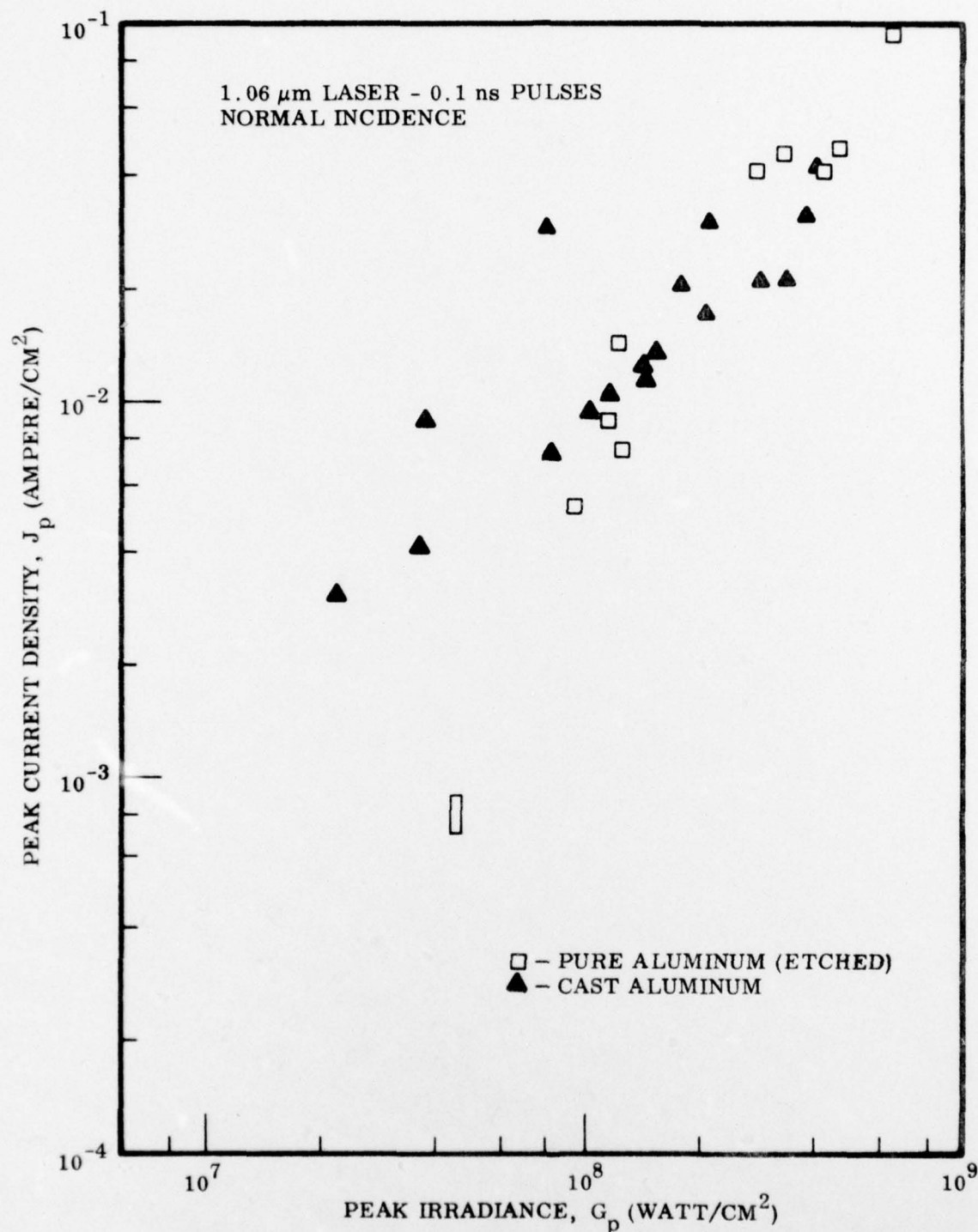


Fig. 4-7. Dependence of Electron Emission on Laser Irradiance
Single pulses of 125 ± 25 ps duration were selected from a mode-locked, Q-switched train and focused to a 1.5 mm diameter spot. Target materials were high purity aluminum and cast aluminum.

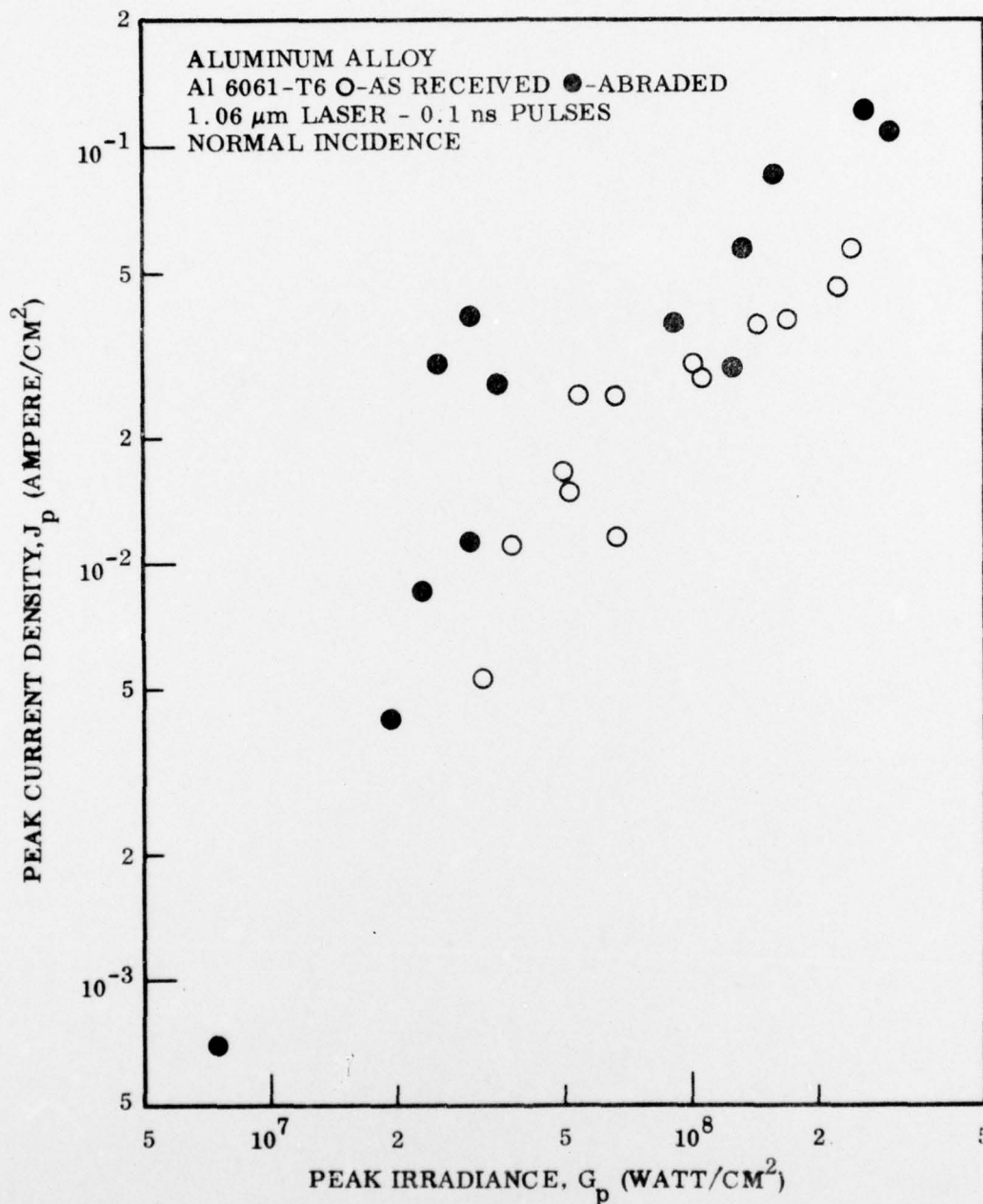


Fig. 4-8. Dependence of Electron Emission on Laser Irradiance. Target materials were "as received" and abraded targets of Aluminum 6061-T6 alloy.

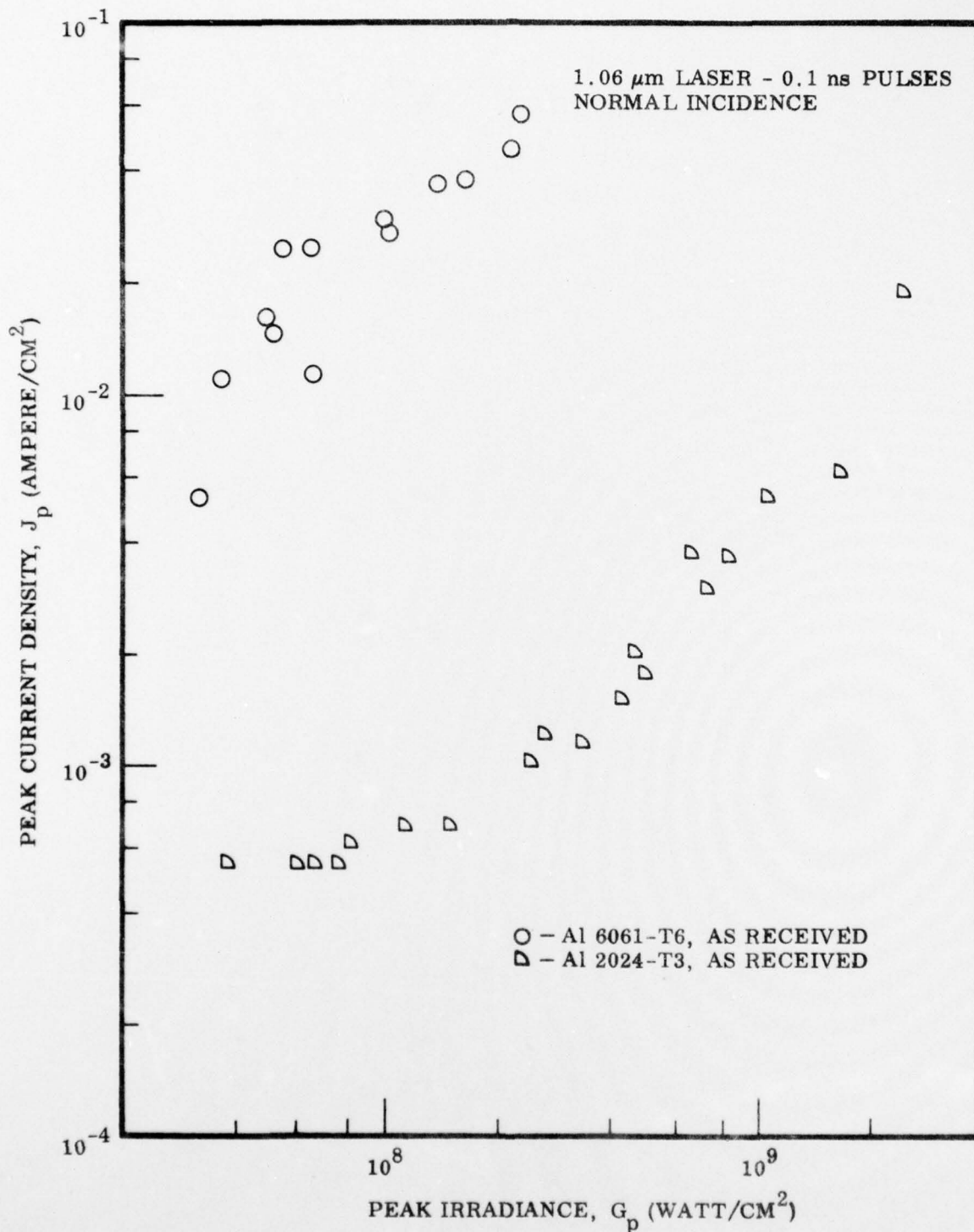


Fig. 4-9. Dependence of Electron Emission on Laser Irradiance.
Target materials were "as received" aluminum
6061-T6 alloy and "as received" aluminum 2024-T3 Alloy

heat treatment in the production of the alloy or to the metallic alloying materials.

In Figure 4-9 the electron emission from two different "as received" alloys is shown. The emission from Al 2024-T3 is nearly a factor of 50 smaller than that from Al 6061-T6. These results indicate that the probability of formation of an LSD wave from a target of Al 2024-T3 alloy should be considerably less than that from pure Al, cast Al, or 6061-T6 alloy.

4.3 Discussion

To examine the experimental results in terms of the possible electron emission mechanisms, one has to evaluate some related quantities. First, a rough estimate is made of the electron current density needed to initiate an LSD wave in air, and the experimental results are compared with the estimate. Next the temperature rise at the target is calculated by two different models, 1) deposition of laser energy into the electromagnetic skin depth without conductive heat loss, and 2) deposition of laser energy at the target surface with heat conduction into the target. The effect of temperature rise on vaporization of the target and upon thermionic electron emission is discussed.

4.3.1 Estimate of Electron Current Density Required to Initiate Fast Breakdown in Air

Walters has shown (Reference 1, November 1973) that a concentration of 10^{14} electrons per cm^3 in air at normal pressure is adequate to initiate fast breakdown in the air as a priming mechanism for ignition of LSD waves by laser pulses. For a mean free path of electrons in air of about $1 \mu\text{m}$ and a buildup time of about 100 ns, one calculates a current density of about $1.5 \times 10^{-2} \text{ A cm}^{-2}$. This number can be compared with the emitted electron current density measured in vacuum in the present experiments as a necessary

but not sufficient condition for initiation of LSD waves in air.

Examination of the CO_2 laser data on stainless steel in Figure 4-1 shows this criterion is met at an irradiance of about $4 \times 10^6 \text{ w cm}^{-2}$, within the range of reported LSD wave threshold irradiance values. Extrapolation of the CO_2 laser data for titanium alloy in Figure 4-2 shows the criterion would be met at an incident irradiance of about $6 \times 10^6 \text{ w cm}^{-2}$, somewhat higher than the reported LSDW threshold of about $2 \times 10^6 \text{ w cm}^{-2}$.

Examination of the Nd laser data in Figures 4-7 to 4-9 shows the criterion to be met at irradiances of about $2 \times 10^8 \text{ w cm}^{-2}$ for cast aluminum and pure aluminum, about $5 \times 10^7 \text{ w cm}^{-2}$ for Al 6061-T6 alloy (somewhat lower for abraded alloy), and at the much higher value of about $2 \times 10^9 \text{ w cm}^{-2}$ for Al 2024-T3 alloy.

These data generally demonstrate that irradiances of the magnitude reported to produce LSD waves in air generate sufficient electron current density to account for the LSD wave initiation.

4.3.2 Temperature Rise at the Target Surface

The calculation of maximum temperature rise at the target indicates the relative importance of thermionic emission and vaporization as sources of electrons.

A simple calculation may be made by assuming that the laser energy is deposited within the electromagnetic skin depth of the target and that no energy is conducted or radiated away. This gives an upper limit to the temperature rise in degrees C

$$\Delta T_m = \alpha (\Delta E) / (\delta \rho c_p) \quad (4.1)$$

where α is the absorptance, ΔE is the incident fluence in the laser pulse in J cm^{-2} , δ is the deposition depth in cm, ρ is the target density

in g cm^{-3} , and c_p is the specific heat capacity of the target in $\text{J cm}^{-3}\text{C}^{-1}$.

Musal (Reference 24) has used Hagen-Rubens theory and experimental measurements to derive the absorptance and electromagnetic skin depth in terms of the electrical resistivity of the metal target and the wavelength of the laser light. He obtained

$$\alpha = 3.65 \times 10^{-2} (\rho_e / \lambda)^{1/2} \quad (4.2)$$

$$\text{and } \delta = 2.91 \times 10^{-7} (\rho_e \lambda)^{1/2} \quad (4.3)$$

where α is the absorptance, δ is the skin depth in cm, ρ_e is the electrical resistivity in ohm cm, and λ is the laser wavelength in μm .

Using this formulation in the preceding equation one obtains for the upper limit to the temperature rise

$$\Delta T_m = 1.25 \times 10^5 \Delta E / (\rho_e \lambda) \quad (4.4)$$

This expression is independent of the electrical resistivity of the metal which cancels out in the term α/δ . It should be reemphasized that the temperature rise calculated from this equation is an overestimate because no energy loss from the laser spot is included in the model. This is labeled Model 1.

Table 4-1 gives the calculated upper limit to the final temperature in various materials starting at 20°C for two typical laser pulses in these experiments, 10^8 W cm^{-2} for 0.125 ns at $1.06 \mu\text{m}$ (Nd laser), and 10^6 W cm^{-2} for $0.3 \mu\text{s}$ at $10.6 \mu\text{m}$ (CO_2 laser).

Model 2, which includes conduction, has been developed by Bechtel (Reference 14). He considers a laser pulse, gaussian in time and space, which is absorbed at the surface of the target. His equations can be

Table 4-1. Properties of Target Materials and Estimates of Temperature Rise

Target Material	Al pure	Al Alloy 6061-T6	Al Alloy 2024- T3	Stain- less Steel 321	Ti Alloy 6Al-4V	
Density	2.70	2.77	2.70	8.0	4.47	g/cm ³
Heat Capacity	0.90	0.84	0.96	0.50	0.61	J/(gC)
Thermal Conductivity	2.37	1.52	1.62	0.16	0.13	w/(cm C)
Electrical Resistivity	2.8	5.74	4.11	70	150	μΩ cm
Absorptance (1.06 μm)	0.060	0.085	0.072	0.30	0.45	
(10.6 μm)	0.020	0.027	0.023	0.09	0.13	
Skin Depth (1.06 μm)	0.5	0.72	0.6	2.5	4	(x 10 ⁻⁶ cm)
(10.6 μm)	1.6	2.3	1.9	8	12	(x 10 ⁻⁶ cm)
Melting Range	660	580- 650	500- 640	1370- 1430	1540- 1650	C
Boiling Point	2467				3287 (pure Ti)	C
Final Temperature						
Nd laser pulse (10 ⁸ w/cm ² , 0.125 ns)						
Model 1	630	660	595	395	565	C
Model 2	47	67	56	410	812	C
CO ₂ laser pulse (10 ⁶ w/cm ² , 0.3 μs)						
Model 1	1480	1550	1390	910	1320	C
Model 2	24	27	26	78	132	C

Model 1. Absorption into skin depth, no conduction or radiation.

Model 2. Absorption at surface, conduction into material.

Values from Reference 22.

simplified to yield the peak temperature at the center of the laser spot

$$T = 1.21 \frac{\alpha I_m}{(K\rho c_p)^{1/2}} \tau^{1/2} \quad (4.5)$$

where α is the absorptivity, I_m is the maximum irradiance incident on the target, τ is the temporal gaussian scaling factor ($= .60$ FWHM), K is the thermal conductivity, ρ is density, and c_p is the specific heat capacity of the target. The temperature rise calculated from this model is also expected to be an overestimate because the laser energy is deposited at an infinitely thin layer at the surface, rather than being absorbed in the volume of the target. (Bechtel also treats the volume absorption case, but the simpler approach should suffice here.) The temperature rises for various materials calculated from Eq. (4.5) is shown in Table 4-2 for the same laser pulses used previously. The temperature increases are significantly lower for most of the cases calculated, but especially for the relatively long CO_2 laser pulses where ample time is allowed for conduction of heat away from the target spot.

The temperature increases above the 20 C starting temperature scale directly with laser irradiance in both models.

Incidentally, at the melting point of metals, the thermal conductivity drops sharply and the electrical resistivity (and hence both the absorptance and skin depth) increases sharply. For pure liquid Al at 700 C the electrical resistivity is 26.3 micro-ohm cm (compared with 2.37 micro-ohm cm at room temperature) and the thermal conductivity is $0.90 \text{ w cm}^{-1}\text{C}^{-1}$ (compared with $2.37 \text{ w cm}^{-1}\text{C}^{-1}$ at room temperature). (Reference 23). Model 1 of temperature rise considered above is unaffected by this discontinuity because thermal conduction is prevented and the electrical resistivity cancels out in the expression α/δ . Model 2 will show increased temperature rises if the target melts because of the reinforcing factors of increased absorptance and reduced thermal conductivity.

4.3.3 Effects of Temperature Rise

The data obtained for 0.1 ns pulses of 1.06 μm laser radiation is considered with respect to temperature rise. At the lowest irradiances, $3 \times 10^7 \text{ w cm}^{-2}$ the electron emission appeared in a short pulse whose width corresponded to the minimum response time of the electronics. As the laser irradiance was increased, this sharp spike of electron emission developed a tail at longer times. At the highest irradiances, $3 \times 10^8 \text{ w cm}^{-2}$ the electron emission pulse loses its "spike" appearance and exhibits both a slower rise and a longer decay. This behavior was observed for all the materials tested. The calculation of temperature rise by Model 1 also supports the suggestion that the dominant electron-emitting process shifts from a prompt emission mechanism to a delayed emission mechanism. Alternatively, a space charge effect might also occur at the higher current densities, limiting the rate of rise of the electron emission pulse and extending its length. This could be tested by increasing the electron drawout field. Assuming zero thermal conduction, the final temperature of the Al 6061-T6 alloy irradiated with a 0.125 ns pulse at $3 \times 10^8 \text{ w cm}^{-2}$ would be 1940 C. This value is considerably below the boiling point of pure Al at 2467 C, so that vaporization even of thin laminae ($0.5 \times 10^{-6} \text{ cm}$) is negligible.

The amount of thermionic emission may be estimated from Richardson's equation (Reference 25)

$$J = A T^2 \exp(-\phi/kT) \quad (4.6)$$

where J is the electron current density in A cm^{-2} , ϕ is the work function of the surface, T is the temperature in kelvins, k is Boltzmann's constant = $8.62 \times 10^{-5} \text{ eV K}^{-1}$, and A is Richardson's constant = $60.2 \text{ A cm}^{-2} \text{ K}^{-2}$. Taking a work function of 4.08 eV for aluminum, one calculates that a surface temperature of 1940 C will produce an electron current density of $1.5 \times 10^{-1} \text{ A cm}^{-2}$, a value in reasonable agreement with that observed for abraded 6061-T6 alloy. The stringent assumption of zero heat conduction was

required to obtain this agreement. Because of the extremely rapid falloff of thermionic emission as the temperature is reduced, thermionic emission is inadequate to account for the observed emission current density at lower irradiances for the Nd laser. For example, at an irradiance of $2 \times 10^8 \text{ w cm}^{-2}$ the calculated final temperature is 1300 C for which the thermionic electron current density is only $1.3 \times 10^{-5} \text{ A cm}^{-2}$.

Failure to observe appreciable electron emission with the longer CO_2 laser pulses on pure aluminum indicates that the temperature rise calculated in the absence of thermal conduction is an overestimate. For example, the temperature rise for a CO_2 pulse of $0.3 \mu\text{s}$ at an irradiance of $1.5 \times 10^6 \text{ w cm}^{-2}$ is 2190 C which would give thermionic emission in excess of 1 A cm^{-2} . Experimentally, an upper limit of $8 \times 10^{-5} \text{ A cm}^{-2}$ was obtained. Consequently, the true temperature rise must be much less.

For these calculations it must be noted that the value of the work function is highly dependent on surface condition so that a variation of several tenths of an electron volt from the quoted value is not at all unreasonable.

4.3.4 Multiphoton Emission of Electrons

The energy of a Nd laser photon of wavelength $1.06 \mu\text{m}$ is about 1.17 eV while that of a CO_2 laser photon is 0.117 eV. Assuming the work function of the metal targets to be in the range 3.6 to 4.6 eV, one calculates that multiphoton photoemission of electrons by the Nd laser is a 4-photon process, while multiphoton photoemission of electrons by the CO_2 laser requires in excess of 30 photons. For true multiphoton photoemission, log-log plots of electron emission current density versus irradiance should have a slope corresponding to the number of photons required (see Fig. 2-1). Examination of the total emission data in Figures 4-1, and 4-6 to 4-8 shows slopes of approximately one and in Figure 4-2 a slope of about two. On this basis the pure multiphoton photoeffect appears to be negligible. It is possible that the measurements reported herein lie in the saturation region of Figure 2-1,

but this is not clearly established.

4.3.5 Enhanced Field Emission

The evidence for enhanced field emission is summarized. Electron emission appears to be prompt except at the highest irradiances (Figure 4-4). Emission is obtained with short laser pulses of high irradiance but low fluence, so that the target is not heated to thermionic emission temperatures and does not vaporize. Polarization of the laser beam normal to the target surface substantially enhances electron emission compared with polarization parallel to the surface in the case of Al 6061-T6 alloy (Figure 4-5), but this polarization effect does not appear for the cast aluminum target. Roughening the target surface produces enhanced electron emission (Figure 4-8 and Section 4.1.3).

Comparison with Table 2-1 shows all these effects, with the exception of lack of polarization dependence for cast aluminum, are characteristic of the enhanced field emission mechanism.

4.3.6 Conclusions

In the experiments reported here, sufficient electron current density to produce LSD waves in air is generated in vacuum at laser irradiances near the reported thresholds. The temperature rise is too small for thermionic emission to be significant except possibly at the highest irradiances studied. The temperature rise is too small to induce vaporization of even thin laminae of the bulk material. The slope of log total electron emission versus log irradiance plots is too small to correspond to true multiphoton emission of electrons. The bulk of the evidence supports enhanced field emission as an operative mechanism for electron production in most of the materials studied.

Section 5
REFERENCES

1. C. T. Walters and R. H. Barnes, "An Investigation of Mechanisms of Initiation of Laser-Supported Absorption (LSA) Waves", Battelle Columbus Laboratories, Semiannual Reports (November 1973, June 1974) with R. E. Beverley, III, Semiannual Report (January 1975) and Final Report (September 1975).
2. P. D. Thomas, H. M. Musal, "A Theoretical Study of Laser-Target Interaction," Lockheed Missiles and Space Co., Inc., a) Midterm Technical Report D313142, December, 1972; b) Final Technical Report, D352890, August, 1973.
3. P. D. Thomas, H. M. Musal, and Y. S. Chou, "Laser Beam Interactions - Part II," Lockheed Missiles and Space Co., Inc., a) Midterm Technical Report D401354, April, 1974; b) Final Technical Report D403747, August, 1974.
4. Gy. Farkas, I. Kertesz, Zs. Naray, and P. Varga, "On the Intensity Dependence of the Non-Linear Electron Emission from Silver Induced by a High Power Laser Beam," Phys. Lett. 24A, 475-476 (1967). Farkas-67b.
5. Gy. Farkas, I. Kertesz, and Zs. Naray, "Discrimination of Laser Induced Nonlinear Photoeffect from Thermionic Emission by Time Response Measurements," Phys. Lett. 28A, 190 (1968).
6. Gy. Farkas, Zs. Naray, and P. Varga, "Dependence of Non-Classical Electron Emission from Metals on the Direction of Polarization of Laser Beams," Phys. Lett. 24A, 134-135 (1967). Farkas-67a.

7. Gy. Farkas, I. Kertesz, Zs. Naray, and P. Varga, "On the Laser-Induced Non-Linear Photoelectric Effect in Metals," Phys. Lett. 25A, 572-573 (1967). Farkas-67c.
8. Gy. Farkas, Z. Gy. Horvath, and I. Kertesz, "Influence of Optical Field Emission on the Non-Linear Photoelectric Effect Induced by Ultra-Short Laser Pulses," Phys. Lett. 39A, 231-232 (1972).
9. W. L. Knecht, "Initial Energies of Laser-Induced Electron Emission from W," Appl. Phys. Lett. 6, 99-100 (1965).
10. E. M. Logothetis and P. L. Hartman, "Three-Photon Photoelectric Effect in Gold," Phys. Rev. Lett. 18, 581-583 (1967).
11. S. R. Ahmad and D. Walsh, "Photoelectric Emission from Metal Surfaces," J. Phys. D: Appl. Phys. 5, 1157-1159 (1972).
12. J. H. Bechtel, W. L. Smith, and N. Bloembergen, "Two-photon Photoemission from Metals Induced by Picosecond Laser Pulses," Phys. Rev. B15, 4557 (1977).
13. J. H. Bechtel, W. L. Smith, and N. Bloembergen, "Four-Photon Photoemission from Tungsten," Optics Comm. 13, 56 (1975).
14. J. H. Bechtel, "Heating of Solid Targets with Laser Pulses," J. Appl. Phys. 46, 1585 (1975).
15. A. A. Boni, F. Y. Su, P. D. Thomas, and H. M. Musal, "Theoretical Study of Laser-Target Interactions," Science Applications, Inc., Final Technical Report SAI 77-567LJ, 1 May 1977.
16. G. L. Matthaei, L. Young, and E. M. T. Jones, Microwave Filters, Impedance-Matching Networks, and Coupling Structures, (McGraw-Hill, New York, 1964).

17. T. S. Green and G. A. Proca, Rev. Sci. Instrum. 41, 1409 and 1778 (1970).
18. R. H. Herz, The Photographic Action of Ionizing Radiations, (Wiley-Interscience, New York, 1969) p. 171.
19. M. Galanti, R. Gott, and J. F. Renard, Rev. Sci. Instrum. 42, 1818 (1971).
20. P. Felgett, Month. Nat. Royal Astron. Soc. 118, 398 (1958).
21. H. Kogelnik and T. Li, Proc. IEEE 54, 1312 (1966).
22. "Aerospace Structural Metals Handbook", AFML-TR-68-115, Air Force Materials Laboratory, Wright-Patterson Air Force Base, Ohio, 1975.
23. J. F. Ready, "Effects of High-Power Laser Radiation", (Academic Press, New York, 1971) pp 130, 132.
24. H. M. Musal, "Laser Radiation, Reflection and Absorption at Metal Surfaces," Lockheed Missiles and Space Co., Inc., Report D560153, June, 1977.
25. R. W. Powell, R. P. Tye, and S. C. Metcalf, "The Thermal Conductivity of Pure and Alloyed Aluminum II. Molten Aluminum and an Aluminum Alloy" in Advances in Thermophysical Properties at Extreme Temperatures and Pressures, American Society of Mechanical Engineers (New York, 1965) pp 289-296.